Modes of propagation and deposition of a landslide onto an erodible substrate: experimental, analytical and numerical study

Crosta, G.B.[1], De Blasio, F.V.[1], De Caro, M.[1], Volpi, G.[1] Imposimato, S.[2], Roddeman, D.[2]

[1] Dept. of Earth and Environmental Sciences, Università degli Studi di Milano Bicocca, Milan, Italy

[2] FEAT, The Netherlands

An erodible substrate and a sharp slope break affect the dynamics and deposition of long runout landslides. We study the flow evolution of a granular mass (1.5-5.1 litres of sand or gravel) released on a bilinear chute, i.e., an incline (between 35° and 66°) followed by a horizontal sector, either sand-free or covered (1-2 cm thick sand layer). Monitoring the time evolution of the falling mass profiled at 120 Hz, the impact dynamics, erosion of the basal layer, and modes of deposition are studied. The frontal deposition is followed by a backward propagating shock wave at low slope angles (<45°), or by a forward prograding flow at greater angles. Experiments with colored sand layers show a complex sequence of dilation, folding and thrusting within both the collapsing sand flow and the substrate. Experimental results are compared with real rock avalanche data and nearly vertical collapses. The observed increase of the drop height divided by the runout (H/L or Heim's ratio) with both chute slope angle and thickness of the erodible substrate, is explained as an effect of vertical momentum loss at the slope break. Data suggest a complex evolution, different from that of a thin flow basal shear flow.

To provide an approximate explanation of the dynamics, three analytical models are proposed. Erosion of a 1 cm-thick substrate is equivalent to 8-12% increase of the apparent friction coefficient. We simulate the deposition and emplacement over an erodible layer with a FEM arbitrary Lagrangian Eulerian code, and find a remarkable similarity with the time evolution observed in the experiments. 2D models evidence the internal deformation with time, 3D models simulate deposition. Capabilities and limitations of an elasto-plastic Mohr Coulomb approach for material modeling are discussed.

Keywords: granular flow, erosion, slope break, physical modeling, rock avalanche, snow avalanches, numerical modelling

1. Introduction

Although it is well known that landslides can be strongly controlled in their evolution and final morphology by the characteristics of the ground surface on which motion and deposition occur, i.e., hard rock versus an erodible substrate, field studies and experiments on the effect of an erodible substrate beneath a landslide have been scarce. In fact, the erodible substrate often remains completely covered underneath the landslide mass, which makes a closer examination difficult (Hewitt, 2006; von Poschinger and Kippel, 2009; Dufresne, 2012). In some cases, however, the erodible substrate has been pushed ahead of the landslide, and traces of substrate flow may still be visible (Choffat, 1929; Jaboyedoff 2003; Crosta et al., 2008, 2009) and recorded by the deformed sediments piled up in arched ridges and grooves.

Ancient rock avalanches may still show the evidence of having been affected by an erodible substrate (McSaveney et al., 2000). The possibility that such a substrate behaves like a lubricating layer has been invoked to explain the extraordinary mobility of ancient landslides on Earth (e.g. Flims rock avalanche, von Poschinger, 2006) and on Mars (Lucchitta, 1979; De Blasio, 2011).

The substrate can be entrained, dragged, sheared, ploughed, bulldozed by the landslide, or may even remain unaffected if the base of the landslide is decoupled from the substrate due to the presence of a basal lubricating layer taking up the shear. Momentum conservation applied to the overall mass (landslide plus entrained material) will cause the landslide to lose speed compared to the case with no entrainment, at least for slopes below critical slope values (ca. 16° according to Farin et al., 2014). So a key question related to the hazard potential of such events is if will be more dangerous because of the increased volume and mobility or less dangerous because entrainment tends to decrease its speed. The physical processes occurring during erosion and entrainment of an erodible substrate have not, however, been studied systematically.

Numerous experiments have been performed as a small-scale analog for landslides and rock avalanches (Denlinger and Iverson, 2001; Forterre and Pouliquen, 2008; Lacaze et al., 2008; Lajeunesse et al., 2004, 2005; Mangeney et al., 2007, 2010; Crosta et al., 2008, 2013b; Manzella and Labiouse, 2008, 2013; Farin et al., 2014). Most experiments are based on the flow of a granular medium along a flume under controlled conditions and involve monitoring of the flow velocity, evolution of the travelling mass, and the examination of final deposit geometry and runout (e.g. Gray et al., 1999; Pudasaini and Hutter, 2006). Most experiments are conducted on a 2-3 meters long flume. Some tests on a larger scale show that the results are nearly independent of the size of the experimental apparatus (Okura et al., 2003). Despite the commonness of landslides travelling on antecedent sediment, comparatively few experiments have addressed the problem (Crosta et al., 2008, 2009; Mangeney et al., 2010; Rowley et al., 2011; Dufresne, 2012; Farin et al., 2014). Rowley et al. (2011) completed a set of systematic experiments where a released mass (ballotini) interacted with another horizontal layer of ballotini deposited on a 5° slope. They measured comparable runouts when changing the release volume at a fixed slope angle (35°), and observed the formation of inverted stratigraphic structures in the final deposits. These are explained by the authors as Kelvin-Helmoltz instability connected to changes in density and velocity between two granular materials in contact. Mangeney et al. (2010) and Farin et al. (2014) studied experimentally the effect of dry sand lying on a sloping ground on the runout of granular flows. They demonstrated that under different conditions and preparation modes of the basal layer (e.g. degree of compaction), the runout may

74 increase even on a very thin erodible bed. This longer runout is associated with higher flow velocity
75 during the deceleration and slow propagation phases.
76 In this work, a joint experimental, theoretical, and field analysis work is set up to investigate the effect
77 of an erodible substrate on the motion of a landslide The process of interaction of a landslide
78 travelling on an horizontal erodible substrate with a small-scale granular flow released onto a sand
79 layer is simulated in a setting similar to the one adopted by Rowley et al. (2011). The experiments
80 are recorded with high-speed cameras and the time-dependent evolution of the landslide is
81 measured with precision.
82 The adopted bi-linear slope geometry allows for a more controllable experimental setting and it is
83 compatible with landslides collapsing onto alluvial plains where an erodible substrate is most likely
84 to be present. This geometry allows also to investigate the influence on the propagation of the
85 granular mass of the presence of an abrupt break of slope. Numerous rock avalanches have spread
86 along simple bilinear profiles (Fig. 1h, 1i): in Tien Shan Mts. (Strom, 2006); the Elm rock avalanche
87 (Heim, 1882; 1932, Hsu 1975); the Frank rock avalanche (McConnell and Brock, 1904); Las Colinas,
88 El Salvador (Crosta et al., 2005); and Arvel, Switzerland (Choffat, 1929, Jaboyedoff, 2003, and
89 Crosta et al., 2008, 2009) and along many Martian slopes, (Lucchitta, 1979). The slope geometry,
90 the scar size and the presence of basal erodible substrate probably did not allow for a steady flow
91 condition to fully develop in all these cases.
92 Different classes of models (Pastor et al., 2014) have been proposed in the literature to study the
93 runout of fast moving landslides. Empirical and semi-empirical models are based on direct field
94 observations and easily measurable variables. Okura et al. (2000, 2003) proposes an approach
95 based on the energy line method for a sledge-like model in which vertical component of the kinetic
96 energy is lost at the impact occurring when a landslide passes thorough an abrupt slope change.
97 The same approach was adopted by Crosta (1991, 1994) to simulate the loss of energy in similar
98 geometrical conditions or when a rockslide-rockfall impacts at the base of a steep rocky cliff. This
99 approach fits well the loss of mobility (i.e. decrease in runout) in presence of geometrical constraints.
100 Lied and Bakkeoi (1980) proposed a simplified semi-empirical model for snow avalanches ($\alpha\beta$-

model) to predict the runout distance based on distance at which the avalanche path makes an angle of 10° with respect to the horizontal.

Mathematical models include different levels of complexity and adopt different approaches in the solution. Depth averaged models have been frequently used to simulate long runout granular flows including levee deposition, basal erosion, pore pressure generation and dissipation (e.g. Iverson, 2012; Pastor et al., 2009; 2014; Mangeney et al., 2007). DEM (Discrete Element Method) models have an enormous potential in the simulation of granular flows even if still prohibitive in simulating extremely large number of particles (Calvetti et al., 2000; Staron, 2008; Taboada and Estrada, 2009). Models adopting depth-integrated conservation equations, generalized from shallow-water theory, have been improved to include erosion of a basal layer according to simplified or more complex models (e.g., De Blasio et al., 2011b, Iverson and Ouyang, 2015). DEM models can directly simulate the interaction between the flowing granular mass and the erodible basal layer or intense shearing allowing for the analysis of internal structures (Taboada and Estrada, 2009), the estimate of the pressure acting on obstacles (Utili et al., 2015) or the interaction with fluids (Zhao et al., 2015). A third approach is with finite elements methods (Chen et al., 2006; Roddeman et al., 2008; Crosta et al., 2009) . In this work, observations attained by laboratory scale physical models (see Crosta et al., 2015a) are used to develop a series of simple analytical models. As a second step, the prediction capabilities of a numerical finite element method with a combined Eulerian-Lagrangian FEM ALE model and elastic-plastic constitutive laws are verified. This yields additional information which cannot be determined directly from the laboratory experiments (e.g., the evolution of internal deformation). Finally, ome of the dynamical phenomena associated to the flow evolution and deposition under the effect of an abrupt slope change are addressed by relatively simple analytical models.

2. Experiments

2.1. Experimental setup

2.1.1. Experimental apparatus

128 The experimental setup consists of two smooth wooden boards (1200 mm long and 600 mm wide):
129 one with adjustable slope angles (30° to 65°, see Fig. 2 for setting and size), is positioned next to a
130 second horizontal board which can be covered with an erodible substrate of dry sand. An angle
131 greater than 65° would result in a nearly head-on impact against the lower sand-covered plate, while
132 a slope of less than 30° is insufficient for flowage. A wooden box (300 mm long, 150 mm wide and
133 160 mm high) containing the granular material is fixed at the upper end of the inclined board at a
134 fixed distance from the upper end of the board, ensuring that a descent length of 900 mm is invariable
135 for different experiments. The down-slope end of the box is closed with a mechanical gate whose
136 opening is controlled by two springs to release the material. The gate opening time is much shorter
137 than the collapse time of the granular material, which ensures a negligible bias on release of the
138 material, as checked through multiple testing and high speed video recording.
139 The inclined board is connected to a smooth horizontal board which may be sand-free, or covered
140 by an erodible sand layer (Fig. 2) with different thickness (10 to 20 mm). Two Plexiglas side boards
141 allow a direct observation of the experiment from the sides but do not cause any lateral confinement
142 of the released sediment volume (i.e. 1.5 to 5.1 litres).
143

144 2.1.2. Methods

145 The granular material in the release box and the erodible sand layer were prepared by hand avoiding
146 uneven compaction. Hand pouring (pluviation) was performed to control the fall height of the sand.
147 Leveling of the deposit was checked and completed by dragging a rigid wooden stick running along
148 lateral supports of fixed height (10 and 20 mm). In order to verify material bulk weight and total
149 released mass, the material in both the release box and in the basal layer was weighed (Table 1).
150 The tests were performed in controlled environmental conditions with constant temperature and
151 relative humidity, and the material was routinely substituted in successive tests.
152 The mechanical parameters of interest to these experiments (Table 1) have been assessed by three
153 methods:

(1) Angle of repose – deposition of sand/gravel cones on different roughened surfaces (smooth or sanded wooden boards) and surveying their geometry and inclination using a high resolution laser scanner;

(2) Angle of avalanching - inclining a board with a homogeneous sand layer until avalanching was observed;

(3) Internal friction - by direct shear testing (ASTM D3080 / D3080M-11) of the materials, and by triaxial test results available in the literature about the Hostun sand.

To verify the repeatability of the results, a series of preliminary experimental runs were carried out more times in identical conditions for different slope angles, with and without the erodible sand layer on the horizontal board. The fact that the variation in runout was at most of the order $\pm$ 2%, made us confident on the statistical soundness of our experimental results. These were followed by a series of tests during which the time evolution of deposition was monitored.

Two high speed cameras (60 frames/s and 600 frames/s) and a laser profilometer (Riegl VZ1000, sampling frequency:120 Hz; beam diameter: 5mm; accuracy: 5 mm and precision: 6 mm, at the test distance ranging between 2 and 4 m) placed in front of the apparatus are used to monitor the flow and capture the landslide evolution in space and time. This allows the propagation velocity of the front to be calculated during different phases of the experiments, which have a total duration of 1 to 1.5 seconds.

2.1.3. Materials

The materials used in the experiments consist of uniform Hostun silica sand (coefficient of uniformity, $D_{60}/D_{10} = C_u = 1.57$; $D_{50} = 0.32$ mm; mean bulk density = 1.42 g/cm^3, min bulk density: 1.25 g/cm^3; max bulk density 1.61 g/cm^3, according to ASTM D7263 - 09 particle density = 2.65 g/cm^3). This was used for both the released mass and the erodible substrate. In some of the experiments, angular/subangular gravel ($C_u = 1.56$; $D_{50} = 7{,}5$ mm; mean bulk density = 1.53 g/cm^3) was released, keeping the Hostun sand for the erodible substrate. Figure 3 shows the grain size distribution curves of the materials together with main grain size descriptors. In another set of experiments, the same

sand on the erodible substrate is colored in stacked layers to explore deformation features associated to the collapse, scraping and thrusting of the erodible substrate. Repeated laboratory testing showed that the colored sand maintained the same physical mechanical characteristics as the ordinary sediment.

2.2. Experimental results

The experimental results and observations are presented for different slope angles and materials (Table 2) in the following order: morphology of the deposit, internal deposit structures, evolution in time of the flow and deposition along the horizontal board.

2.2.1. Bulk experimental deposit

Figure 4 shows the patterns of experimental deposition for some of the runs with different slope angles θ (40°, 55° and 66°), with and without the erodible basal layer, and for different release volumes (1.5 and 5.1 litres). These cases have been chosen because they represent well the most important and commonly observed features that will be described in the following.The total runout is found to decrease with the slope angle, whereas the ruonut along the horizontal part of the path increases. At lower slope angles, a thick bulk deposit forms at the slope break characterized by a series of transversal grooves and furrows. In the case of a smooth surface and high slope angle (Fig. 4g), the tail of the deposit detaches completely from the sloping ground, and produces a very elongated apron deposit. The presence of the basal erodible substrate decreases the runout and produces a lunate deposits of arcuate form, similar to that of barchans dunes. The proximal deposit (i.e. facing the flow) is steeper, while the distal one is gentler (Fig. 5). A decrease in inclination of the sloping part of the path results in deposits that progressively propagate uphill in a triangular shaped and grooved sedimentation pattern. The inclination of the frontal part of the deposit decreases progressively (22.4° to 14.8°) with the increase in slope angle (e.g. 45° to 60°, see Fig. 5). A much lower inclined front is observed in the case of propagation on a smooth horizontal surface (e.g. 9.8°), whereas the upstream facing side of the deposit is maintained at approximately the same inclination

208 through the various tests (e.g. 16.9° to 17.4° with the erodible substrate and 19.2° on smooth base
209 in Fig. 5). All these values are well below the angle of avalanching as determined by laboratory tests.
210 Furthermore, the smoother superficial morphology of the deposits is well characterized by the slope
211 angle as computed from the slope profile data. For example, in the case of 45° slope with no basal
212 layer, the change in slope angle occurs smoothly along the entire deposit length. Figure 5b
213 evidences the stepped surface geometry of the deposits by a series of peaks in the slope angle
214 values, with constant spacing and amplitude. When coarse gravel is released instead of Hostun
215 sand, the deposit still grows upslope with decreasing slope angle, resulting in a rough conic geometry
216 with the apex aligned with the deposit centerline (Fig. 6). The deposit length increases slightly with
217 the board slope angle. While at low slope angles several isolated particles outrun the deposit front,
218 at steeper angles the interaction with the basal sand layer increases forming a wedge of material
219 pushed or upraised well in front of the coarse material wedge.
220

221 ## 2.2.2. Internal structures of the experimental deposit

222 To visualize the internal geometry of the deposit, in a series of experiments some colored sand
223 layers were inserted in the basal sand using the pluviation technique described earlier. The layered
224 sequence is formed from the bottom up by: a 10 mm thick lowermost layer of uncolored Hostun sand
225 in contact with the basal board; a 3 mm thick layer of orange colored Hostun sand; 5 mm of uncolored
226 Hostun sand; and a 3 mm layer of blue colored Hostun sand (Figure 7). The resulting experimental
227 deposit (Fig. 7a) was wetted to provide the sand with apparent cohesion necessary for cutting
228 sections through it.
229 Figures 7 (b-d) show the deposit and some longitudinal and transversal cuts. The orange layer
230 appears doubled in size in sections both parallel and perpendicular to the direction of flow, while the
231 blue layer, which has been sandwiched between the two, increases in thickness and has upper
232 irregular limit. A lack of both colored layers in the upstream side of the deposit confirms the erosive
233 action played by the granular flow at the slope break. The blue layer is eroded and re-deposited
234 along the basal movement surface. However, the orange layer at the foot of the slope has been

stripped and entrained inside the flow, remaining inside the upper cap of the travelling mass and partially inverting the stratigraphic sequence (orange – blue-orange in Fig. 7e). Closer to the centerline, multiple shear planes with associated thrust fold-like features have been observed in the longitudinal cross cuts. Experiments at lower slope angles, in which the granular flow cannot dig deeply enough into the granular bed, do not result in well-developed layer doubling.

2.2.3. Dynamics

For our dynamical studies, we used two high-speed cameras and a laser scanner. Here we first consider the succession of processes recorded in the experiments (Figs. 8a, b, c); a quantitative analysis of some issues is deferred to later subsections.

Let us first consider the flow of sand without an erodible substrate (Fig. 8a). As soon as the gate is released, sand spreads laterally and longitudinally. After the initial flow along the inclined plate, the front collides with the flat horizontal plate and then travels for some distance. Consequently, as the speed of the front diminishes, the granular flow tail collides against it from behind and single grains leap into ballistic trajectories. At this stage, a backward propagation of a sand shock wave is observed similar to those described by Pudasaini and Kroner (2008). The rear of the deposit shifts backward and upslope almost linearly with time. In this phase, ramp-like features are created similar to those exhibited by landslides (last four frames in Fig. 8a). These features suggest a progressive backward shifting of the deposit center of mass following the halt of the front.

In the presence of the erodible substrate (Fig. 8b), the dynamics becomes more complicated because the initial impact of the avalanche front with the flat plate results in dilation of the granular eroded mass and a progressive excavation of the erodible substrate down to a certain depth. The consequent entrainment increases the mass of the granular flow and delays the progression of the flow compared to the case of no erodible substrate. In the first images of the sequence, the evolution and rapid spreading of a very shallow wave ahead of the larger and steep breaking wave are visible (see Fig. 8b).

Particles approaching the deposit from behind jump at an angle corresponding to the slope of the deposit. This allows to estimate the distance reached by grains and the projection velocity (seesection 3). The fountain of launched particles together with the material set into motion has the form of a dense breaking wave travelling along the top of the granular erodible substrate. However, as the front builds up, it becomes more dense and massive, and finally stops. In addition, the rear part of the deposit becomes a little bit steeper, which impedes the ballistic jump.

The final geometry resulting from the ramp-like deposition and internal deformation is shown in Fig. 9. Erosion and entrainment make the bulk of the deposit stop earlier; however, the later sequence of processes is similar to the case with no erodible substrate. Figure 8c shows the case for a gravel granular flow. Due to the greater mass of the falling particles, the impact induced dilation of the sand layer increases, the erosion is deeper and more material is entrained. Strongly dilated sand of the erodible substrate, set in motion by the incoming gravel, travels ahead of the resulting flow, forming the steep frontal part of the wave and eventually the final deposit, while gravel does not overtake the eroded sand. As the main frontal mass stops, the shock wave propagates upstream in a stepped (ramp-like) mode with a rough pyramidal geometry controlled by the discharge of the flow and volume of the material forming the flow tail.

2.2.4. Accumulation

Based on the analysis of the internal structure observed in tests with colored sand layers and the qualitative analysis of the temporal evolution of the flow and deposition, a three-phase mechanism of flow and deposition is distinguished. In a first phase, the bulk of the granular flow collides with the flat plate. In a second phase, the granular flow causes dilation and erodes the substrate and then leaps in ballistic flight, hitting the top of the deposit with a perturbation in the form of a wave front, which becomes progressively steeper (Fig. 9b) and then gradually loses inclination. In the final stage, and at low slope angles (i.e. θ < 40-45°), the front of the deposit stops flattening out progressively while the rest of the flow, which is still depositing at the rear of the heap, builds up a series of ramp-

like features growing upslope. At higher slope angles, some of the flowing material overpasses the bowed crest of the deposit and generates a gentle leeward side deposit with minor undulations.

To quantitatively analyze this sequence of phases, flow profiles along the model centerline have been monitored at a 120 Hz frequency (at 0.025 s interval, see Figures 9). For all types of tests (Fig. 9) we observe a change of behavior as a function of the slope angle. At 40° angles, the backward propagating shock wave deposits at a constant rate till exhaustion of the flow. At 45°, the behavior starts changing from a backward to a more downward deposition and at 50° and then 60° the rear part of the flow passes over the main mass elongating the deposit (see Fig. 9b sand on sand layer). For the gravel on sand layer experiments, Fig. 9c shows that eroded sand is raised and pushed up in front of the falling gravel mass and extends well beyond the tip of the gravel mass, recognizable in the profiles by the very rough surface. Figure 9d, an enlargement of the 45° case in Fig. 9b (with vertical exaggeration) illustrates the progressive formation of the frontal wave, the steepening front and the successive readjustment of the frontal slope to a gentler angle.

The front velocity reaches a maximum at the beginning of the wave formation, and raises again during the readjustment of the front slope angle (up to a final 21.5° value) before the deposit comes to rest. The Froude's number, computed considering the maximum wave height, shows supercritical flow just at the beginning of the propagation along the sub-horizontal part of the path, which becomes rapidly subcritical during most of the spreading and deposition. In contrast to Pudasaini and Kroner (2008), who feed their system with a continuous steady state flow, these experiments are strongly transient (Fig. 9, 10 and 11). The highest observed values of backward accretion velocity ranges between 0.1 and 0.2 m s^{-1} in our experiments. The interval upon which the shock wave wedge accretes linearly with time is short due to the instantaneous release of the granular medium and the progressive rapid change in sand discharge.

A complete summary of the experimental observations can be attained by plotting the change in elevation along the centerline of the model with time. These spatio-temporal plots provide a clear visualization of the front evolution and of its velocity during the propagation along the horizontal part of the path (Figure 10). Figure 10 shows three spatial-temporal plots for the case of sand on smooth

surface (a), sand on sandy erodible substrate (b) and gravel on sandy erodible substrate (c). On the right hand side of these plots the sloping plane profile and the disturbance in geometry generated by the descending material are reported. The slope of these curved features yields the velocity of the fronts along the plane and in proximity of the impact at the slope toe. The mean terminal velocity computed for the different experimental conditions is plotted in Fig. 11 against the theoretical friction-free fall velocity $\sqrt{2gL'sin\vartheta}$ and the velocity with friction $\sqrt{2\,gL'(sen\theta - cos\theta tan\varphi)}$ where ϑ is the slope angle, φ is the friction angle, g is the gravity acceleration, and assuming different values of the basal friction angle, different slope angles and a constant length of the inclined path *L'=0.9 m*.

When the avalanche front starts its propagation on the horizontal layer (i.e. at the slope toe where the 0 value of the x axis is fixed) the ballistic launch, initial erosion and the front wave formations form a cusp which progressively enlarges with time. This cusp becomes more evident with the increase in slope from which the instantaneous velocity of the flow at different elevations (e.g. the base) is obtained.

In the case of gravel flowing on sand, the propagation of the eroded sand wave in front of the gravel is recognizable by the much smoother surface with respect to that of the gravel material. Starting from these plots, the front position with time has been reconstructed (Figure 12). Sand avalanches on smooth surface are the most mobile followed by the gravel on sand flows for which sand is mobilized by the falling gravelly mass. Sand is much less mobile when spreading on the sand basal layer. Notice that both for sand on smooth surface and for gravel on sand, the longest horizontal runout is measured for the steepest slopes, whereas for the sand on sand the maximum spreading is observed at a slope of 55°. This dynamics differs noticeably from the one observed for propagation along constant slope cannels. The lower runout for eroding granular flows is reflected in the H/L diagram (Fig. 13). In Fig. 13a we show this ratio as a function of the slope angle. Note that data points for the experiments without erodible layer fall below the rest of the other data points. Moreover, the thickness of the erodible substrate directly influences the H/L ratio at different volumes of the granular flow (3.4 l in Fig. 13b and 5.1 l in Fig. 13c).

1. Analysis of flow dynamics

3.1 Mobility

We start the analysis developing a simple analytical solution which describes the runout including the effect of the slope break. A common measure landslide mobility is the tangent of the Fahrböschung (FB), a proxy to the apparent friction coefficient encountered during the flow (Scheidegger, 1973). This is the Heim's ratio H/L between the vertical drop (H) and horizontal spread (L) of the landslide, calculated adopting as initial point the rear end of the mass prior to failure, and as an end point the tip of the deposit. For an experimental mass, this ratio is close to the friction coefficient of the granular-bed interface (Erismann and Abele, 2001) and can be much affected by the aspect ratio of the initial granular mass (Lajeunesse et al., 2004, 2005; Lube et al., 2005; Crosta et al., 2009, 2015a). This is because part of the available energy derives from the initial configuration, rather than flowage downslope. For the tests presented in this study, however, this effect should be minimal because the ratio between the vertical size of the containing box and the vertical fall of the center of mass is very small. The relevance of the landslide geometry has been discussed in detail by Lucas et al. (2014) for a constant slope angle (lower than the friction angle), showing the complex dependency of H/L from various variables. Thus, they define a more effective coefficient of friction ($\mu_{eff} = \tan\theta + H_0/\Delta L$) where the geometry of the initial configuration is accounted for (in our experimental setting a box of length ΔL and thickness H_0). Experiments show a classical relationship between FB and volume, but of limited significance considering the small volumes involved. Moreover, because in these tests the attention was focused on the geometry and characteristics of the flow and deposit along the flat propagation sector (i.e. the valley bottom for many real landslides), the main goal is the relationship between slope geometry and final runout. The dependence on the characteristics (e.g. roughness and stiffness) surface onto which flow occurs is also of great importance (Crosta et al.,2008).

Figure 14 shows the FB of the experimental granular mass as a function of the different slope angles. In all cases, the FB increases with the slope angle. In the following, we explain this effect noticing that at the break of slope most but not all of the vertical component of the momentum is transferred to the earth surface. If the horizontal component of the momentum is conserved at the slope break,

368 and assuming that this component sums up to a fraction ε of the vertical component of the pre-impact
369 velocity where ε is a coefficient of restitution, the absolute value of the velocity past the slope break
370 is:

371 $$U_x = \sqrt{2gL'(sin\theta - \mu cos\theta)}\,(cos\theta + \varepsilon\, sin\theta) \quad (1)$$

372 where L' is the length of the sloping board. The coefficient of restitution accounts for the conversion
373 of part of the vertical to horizontal velocity, the possible decrease in normal force, and is suggested
374 by the irregularity of geological surfaces, clast shapes and observed trajectories. This is because
375 the collision of grains against a horizontal and rough surface results in a velocity component parallel
376 to the surface, even when the initial trajectory is perfectly vertical. A grain, even if falling vertically,
377 acquires after bounce a horizontal component owing to the unevenness of both the grain and the
378 table. Obviously, this does not violate momentum conservation, because the extra horizontal
379 momentum acquired by the grain is compensated by an opposite momentum taken up by the Earth.
380 Along a similar line is the model by Okura et al. (2003) based on full loss of the vertical kinetic energy
381 component. The function $\Theta(\theta) = (cos\theta + \varepsilon\, sin\theta)$ in eq. (1) embodies the effect of the collapse onto
382 the horizontal path. The total horizontal length travelled by the centre of mass (first on the inclined
383 board, then on the horizontal portion) is then

384 $$L = L'\, cos\theta + \frac{U_x^2}{2g\mu} \quad (2)$$

385 and considering that the vertical drop is $H = L'\, sin\theta$, substituting U_x from eq.1 into eq. 2, we find a
386 relationship for the ratio between the total drop height and the runout of the kind:

387

388 $$\frac{H}{L} = \frac{\tan\theta}{1+[cos\theta+\varepsilon\, sin\theta]^2\left(\frac{\tan\theta}{\mu}-1\right)} \quad (3)$$

389 Eq. (3) increases monotonically with the slope angle, implying that, the other conditions being equal,
390 a landslide from a steep terrain loses mobility at the slope break compared to one travelling on a
391 smoothly varying terrain. Note that the standard equation H/L= μ can be retrieved for a unitary value
392 of the function $\Theta(\theta) = 1$ in Eq. (3). It is likely that the coefficient of restitution, considered constant
393 in Eq. (1), will be a function of the angle of impact, increasing for head-on impacts. An alternative

choice could thus be $\Theta(\theta) = (\cos\theta + \varepsilon \sin^2\theta)$. Direct calculation shows however only a slight difference in these approaches.

The fit of the proposed relationship to experimental data is shown in Fig. 14 for experiments on a smooth surface with two different released volumes (3.4 and 5.1 litres). The fact that the granular material enters the flume with non-zero velocity, can be accounted for by substituting the denominator of Eq. (3) with

$$1 + [cos\theta + \varepsilon\, sin\theta]^2 \left(\frac{\tan\theta}{\mu} - 1\right) + \frac{B}{cos\theta\, L'} \qquad (4)$$

where *B* is the height of the released mass along the vertical direction. Because in our experiments the ratio $\frac{B}{cos\theta\, L'}$ is at most 0.15, we neglect its effect.

Starting from Eq. 3 the run-out on the horizontal board can be calculated as:

$$R_H = \frac{L' \sin^3\theta}{\mu}\left[\left(1 - \frac{\mu}{tan\theta}\right)\left(\frac{1}{tan\theta} + \varepsilon\right)^2\right] \qquad (5)$$

which is a convex function of the angle θ. It initially increases for angles slightly greater than the friction angle, and then decreases reaching a minimum value equal to $L'\varepsilon^2/\mu$. The horizontal runout calculated with Eq. (5) is compared to experimental results in Figure 15 for propagation on a smooth surface. Even though the values are not exactly the same, Eq. (5) captures the general trend with a maximum runout on the horizontal surface at about 50°. Clearly the model is not meant to provide a detailed solution as it does not include a volume effect and it refers to the center of mass whereas the experimental data refer to the deposit front.

3.2 Apparent friction in presence of an erodible layer

To clarify the increase of apparent friction coefficient in the presence of the erodible medium, we now introduce a simple model based on the momentum conservation. Let the acceleration of the center of mass of the granular mass along the ramp be described with a friction coefficient $\mu = tan\phi$ in the form

$$\frac{du}{dt} = g(sin\theta - \mu cos\theta) \quad (6)$$

The flow reaches the slope break with a velocity:

$$u_0 = \sqrt{2gL'(sin\theta - \mu\, cos\theta)} \quad (7).$$

In the absence of the erodible substrate (i.e. smooth surface), the velocity as a function of the position x along the horizontal board would be

$$u = \sqrt{u_0^2 cos^2\theta - 2gx\mu} \quad (8)$$

In the presence of the substrate, the granular mass entrains part of the erodible layer down to a depth *D'*. We assume that the areal extent and the density of the eroded layer are the same as the case of the granular flow. Thus, the momentum $M\, u_0$ of the granular flow of mass *M* just before entrainment will be shared between the mass itself and the entrained mass, so that the momentum after entrainment is [$u_{entr}(M+M')$], *where* u_{entr} *i*s the velocity after entrainment

$$u_{entr}(M + M') = Mu_0 cos\theta \quad (9)$$

and

$$M = SD\rho; \quad M' = SD'\rho \quad (10)$$

where S is the basal surface area of the flow, ρ the density of the granular material, D is the flow thickness before entrainment, M' the entrained mass. Thus, in the presence of an erodible layer the velocity as a function of the position is given by

$$u = \sqrt{u_{entr}^2 - 2gx\mu}\ . \quad (11)$$

We find the horizontal spread, R^*_H, of the mass on the flat table in the presence of the erodible layer by putting the argument of Eq. (11) to zero, and using Eqs. (9) and (10) to solve for x. We find that the horizontal spread is diminished with respect to the case of no sublayer (eq. 5, assuming a restitution coefficient equal to 0) and is given as $R^*_H = R_H/(1+D'/D)^2$. This results in a Heim's ratio H/L equal to

$$\frac{H}{L}(D') \cong \frac{H}{L}(D' = 0)\frac{R_H + L'cos\theta}{R_H^* + L'cos\theta} \cong [1 + \frac{2cos^2\theta}{\mu}(sin\theta - \mu\, cos\theta)\frac{D'}{D}] \quad (12)$$

In the above equations, the total runouts in the presence and absence of the erodible layer are $R_H^* + L'cos\theta$ and $R_H + L'cos\theta$ respectively, while the vertical drop, which disappears from the final expressions in (8), is evidently the same for both cases and equal to $L'\, sin\theta$.

445 Numerically, it is found that 1 cm of erodible material results in 8-12% increase of the apparent
446 friction coefficient in our experiments. This implies that if the ratio H/L without erodible bed coincides
447 with the friction coefficient (as it ought to), or about 0.58 corresponding to an angle $\tan^{-1}(H/L)=30°$
448 (see Table 1), 1 cm-thick erodible layer increases the ratio and the corresponding angle to about 32°
449 and 32.6° at slope angles of 40° and 50° respectively, which may explain the results observed in
450 Fig. 13.
451 Note that the apparent friction coefficient appears to saturate as a function of the erodible layer
452 thickness, which indicates a limit D_{MAX} in the depth of granular material that the flow can entrain. This
453 is as also suggested, for different experimental conditions, by Mangeney et al. (2010) and Farin et
454 al. (2014). Thus, if the thickness of the erodible layer D is less than $D_{MAX,}$ the granular flow will tend
455 to erode the whole layer (weathering limited condition). However, if $D > D_{MAX}$ (transport limited
456 condition), only the part of the erodible layer at depth less than D_{MAX} will be eroded and entrained,
457 which limits the friction angle. The existence of a maximum thickness D_{MAX} is reasonable considering
458 that the shear stress necessary to mobilize a granular material increases with the overburden
459 pressure. Although this estimate, given its intrinsic simplifications, cannot be pushed to any better
460 precision, it is clear that momentum conservation during entrainment can account for much of the
461 observed apparent increase of the friction angle as a function of the thickness of the erodible layer.
462

463 ## 3.3. Grains in ballistic flight

464 The flow of grains hitting the rear of the frontal portion of the deposit and jumping in ballistic flight
465 can be analyzed considering the simple kinematic problem illustrated in Fig. 15. The launch velocity
466 will be controlled by the efficiency of the reflection and the friction force mobilized along the ramp.
467 We assume that the rear part of the horizontal sand layer (i.e. close to slope toe) behaves initially as
468 a “reflecting” surface, and after some erosion has taken place, this develops into a natural ramp from
469 which grains may leap. Two extreme cases can be considered. In the first case, the magnitude of
470 the incoming velocity of grains (u_A in Fig. 15) is preserved after collision (u_B) so that only the direction
471 of the velocity vector is changed. At the other extreme, it is assumed that the component of the

velocity of the incoming grain perpendicular to the natural ramp is absorbed by the sand layer, i.e., the normal coefficient of restitution is zero, while the component parallel to the ramp keeps the same velocity corresponding to parallel coefficient of restitution equal to one. In general, the velocity of the grains in position B will thus be a fraction f of the velocity in A, i.e., $u_B = f\,u_A$. The cases $f = 1$ and $f = \cos(\delta+\theta)$ correspond to the first and second state, respectively. They are two extreme cases and it is to be expected that f should fall between these two extremes. The grain then decelerates as it travels against gravity and friction along the natural ramp of height H from which it leaps in ballistic flight (Fig. 15). The inset plot in Fig. 15 shows the total length of ballistic jumps as a function of the coefficient f calculated with elementary kinematics. Note the threshold behavior as a function of the coefficient and the change in ramp length (up to 0.16 m for this example). If $f < f_{CRIT}$, where f_{CRIT} is a critical value of f (as an example, f_{CRIT} is about 0.37 for the case δ=14°; θ=50°; and friction angle 30° illustrated in Fig. 15), the grain has not enough energy to climb up the ramp formed by erosion of the basal layer or piling up of the flowing material. It therefore stops at the rear end of the deposit or erosion groove, in a mode similar to the backward propagating shock wave contributing to building up the deposit. If $f > f_{CRIT}$, the grain has enough energy to rise up the ramp and jump in ballistic flight. Observations suggest a jump distance of the order 80-100 mm, which would correspond to a coefficient f of the order 0.4-0.8.

Verification of the simple model can be achieved by examining the evolution of the backward propagating shock wave. In this phase, the material descending along the slope reaches a velocity controlled by the slope length and inclination, and the coefficient of friction. The velocity after the change in direction (i.e. during the run up along the uphill side of the deposit) is too low and the flow cannot pass the crest of the deposit. The fact that the granular material at low slope angles preferentially accumulates at the rear of the deposit can be understood based on simple dynamic considerations. For the granular flow coming from behind, a certain amount of energy is necessary to overcome the deposit. Calling X the maximum horizontal distance reached by the granular flow on the deposit, it follows that

$$f = \left[\frac{2g(tan\delta+\mu)X}{u_0^2}\right]^{1/2} \quad (13).$$

Because we observe that the X is close to the horizontal length of the upstream side of the deposit, we can compute the value of *f* during the backward shockwave propagation. In the case of a 45° slope this gives an experimental slope angle δ=14° for the upstream side of the deposit, with an horizontal length X ≈ 9 cm, a value of *f* of about 0.8. Again, this value confirms the ballistic jump length observed.

Hakonardottir et al. (2003a, b) carried out a series of experiments where a granular flow of constant depth collided against a dam of given height and inclination angle. They found that when the depth of flow is much less than the dam height, the granular flow upon impact with the dam leaps ballistically with a launch angle equal to the upstream angle of inclination of the dam. This parallels the experimental situation presented here where the dam is substituted by the deposit, whose upstream side is constantly changing shape.

4. Numerical modeling

Numerical models can support the understanding of granular flow evolution both in time and space, and validate the interpretation given for some of the features observed during the experiments. At the same time, they can test some of the assumptions made about the material behaviorNo numerical model results concerning the simulation of such type of processes have been published till now and this motivates the presented set of simulations.

4.1 Numerical method

Because of the large displacements and deformations occurring within a flowing granular material, a Lagrangian finite element method would be subjected to high mesh distortion and inaccuracy. Following previous experience in simulating both small (Crosta et al., 2008, 2009, 2013b, 2015a) and large scale granular flows (Crosta et al., 2005; 2006, 2008, 2013a, 2015b) with different characteristics, the same FEM numerical approach (Roddeman, 2008; Crosta et al., 2009, 2015a, b;) will be used here. The numerical approach is a combined Eulerian-Lagrangian scheme which demonstrated to provide accurate results under various modeling conditions (Crosta et al., 2009,

2015a, b). We assume an elasto-plastic behavior with a standard Mohr-Coulomb yield law, which requires a relatively simple material description. Considering the evidence of a dense flow along the horizontal runout zone (Rowley et al., 2011; Crosta et al., 2015a), this seems a reasonable assumption to be tested through the numerical models. To minimize computational effort we take advantage of the test symmetry with respect to the centerline and model only half of the chute. The released mass (5.1 litres) and the erodible layer (2 cm thick) are assigned the same properties through both 2D and 3D simulations, with an internal friction of 28.5°, no cohesion and dilatancy whereas a friction angle of 22° and no cohesion have been assumed at the interface between the granular medium and the smooth surface. These values are derived from the low side of the experimental tests considering also the possible variability of the internal friction angle during motion and deposition. The adopted isoparametric finite elements are 3-noded triangles in two dimensional simulations and eight-noded hexahedrals in three dimensions.

Boundary and initial conditions are coincident with the experimental ones in terms of lateral confinement and release mode. The initial equilibrium stress state for the granular mass contained in the releasing box is reached through quasi-static time stepping so that no inertial effect is introduced. Then gravity is incrementally applied in successive time steps. The release is simulated by deleting a retaining wall. The dynamic equilibrium equations (Crosta et al., 2009) are then solved for the entire area of the spreading material and without introducing pre-imposed controlling conditions both for the onset and the evolution of the material erosion and deposition. In the following, two sets of results from the simulations are presented, referring to both two three dimensional (50° slope, 5.1 l and 60°, 3.4 l) and one two dimensional experimental layout (66° slope, 5.1 l). This last was performed on a geometry similar to the experimental one, where thin coloured layers were inserted within the erodible layer. For the calculations, 60,814 triangular elements (max size 0.003 m) and 270,380 hexahedral elements (dz = 0.0025 m, dy = dx = 0.01m; 10,210 and 19,410 elements for the landslide and the erodible layer, respectively) were used to discretize space in two dimensional and three dimensional simulations, respectively. The different finite elements size is the result of a compromise between resolution of the models and computing time.

4.2 Numerical results

Three dimensional simulations (Fig. 16 and 17) show the formation of a large snout, its propagation along the slope and successive impact, erosion and deposition phases. After the release of the confining wall, the material starts to flow developing a steep snout at the front and an elongating tail. The final deposit has a lobate geometry with a gentler frontal slope with respect to the upward side (Fig. 16).

In this case the final deposit geometry fits well with the experimental results (Fig. 16 and Fig. 17c, 50°), with a maximum thickness of 8 cm and runout of 110 cm from the upper release limit compared to the experimental values of ca. 7.5 cm and 115 cm. Impact at the slope base occurs between 0.6 and 0.7 s (Fig. 17), with the maximum front velocity of about 2.7-2.9 m s^{-1}. At 0.7 s, the avalanche material undergoes a change in direction with velocity vectors pointing downstream and upward, and the erodible layer is set in motion. At 0.9 s the steep front of the flow runs at high speed. The evolution of the material front during the experiment is reported in Figure 2b, where the position of the front is reported both for the eroded material and the falling mass. These data can be compared to those of the laboratory experiment (50°, 5.1 litres) in the same figure.

3D simulations show the spreading of the flowing mass along the slope as well as the distribution of erosion and deposition (see also Fig. 16). To better investigate the avalanche geometry at and after the impact, the erosion process, and the internal deformation of the erodible basal layer, a 2D modeling approach is more suitable mainly due to the lower computational requirements. At the same time, with these simulations it is possible to test the validity of using a continuous elasto-plastic modelling approach for modelling the erosion and deposition phase both at the laboratory and eventually at larger scales. The 2D simulations (Figs. 16 and Fig. 17) clearly show the generation of a steep front and the jump of the avalanche flow above the basal layer. The basal layer is completely pushed away at the front of the avalanche and starts to be eroded from the surface and folded at depth (Fig. 17a). In Figure 17 f) the decreasing velocity of the material climbing at the front and eroding the layer can be observed, as well as the high velocity of the material still rushing down the slope and pushing the front from the rear. The maximum velocity at impact is about 3.2 – 3.5 m s^{-1}

(see Figs. 17f-l) and comparable to the one computed (eq. 7) assuming a basal friction angle of 25° (3.57 m s^{-1}) and 31° (3.44 m s^{-1}). The upper part of the front starts climbing up against the basal sandy material, along a steep and straight shear band, and overpasses the crest generated in the basal layer. The dragging and pushing of the material continues (Fig. 17b) with the front part composed of the basal material becoming progressively steeper, until an overturn fold starts developing. The front of the avalanche material, slowed by the folding basal layer, collapses backward (Fig. 17g). The fold is completely overturned and the upstream (left hand limb) is torn off, with a thin discontinuous layer of orange and brown sand remaining below the avalanche ramp (Fig. 17c) and the shear plane below the avalanche assumes an S-shaped geometry. At this step the brown layer is completely overturned and doubled in thickness. The velocity vectors (Fig. 17h) suggest at this time a sort of front instability. The final two steps (Figs. 17d and e) are characterized by the elongation of the deposit (see also Figs. 17i and l) and of the S-shaped contact band between the avalanche material and the overturned basal layer. The final front inclination at 21° is compatible with the 22° for the experimental test (see Fig. 16c). It is worth noting that because of the plane strain conditions, the flow reaches the slope toe with a thickness greater than the measured one. As a consequence, the simulated avalanche erodes away a longer part of the basal layer compared to experimental data. Nevertheless, this set of observations fits fairly well to the experimental ones (see Fig. 7 and Fig. 17e, and Fig. 16C)..

5. Discussion

There are numerous cases of landslides (Fig. 1 and Table S1 in Supporting Information) and granular flows occurring along a steep slope followed by a sub-horizontal and planar spreading area. Flat areas often coincide with an alluvial plain made of an erodible substrate.

5.1 Runout

Hutchinson (2002) and Duperret et al. (2006) describe collapses of chalk headwalls (see data in Table S1) onto flat tidal areas in northern Europe. Recognizing that vertical collapses exhibit shorter runouts than those occurring along a gentler slope, Hutchinson (2002) suggests that this is because

608 vertical collapses involve harder and less porous rocks, less prone to water remoulding and loss of
609 strength. However, he also points out that a vertical collapse has a smaller horizontal component of
610 the initial velocity. Table S1 and Fig. 14 report data for rock avalanches with steep slopes and show
611 an increasing trend of H/L with slope angle, as noticed in experiments with large cubic blocks (Okura
612 et al., 2000, 2003). Fig 13a shows the increasing trend with slope angle and with the thickness of
613 the erodible layer, with minimal H/L values for a perfectly smooth and sand free surface (stars), and
614 an opposite trend is recognized with respect to the released volume. Figure 13b and c show the H/L
615 relationship with the sand layer thickness as a function of the type and volume of released material.
616 They show a sort of saturation effect for thicker layers (2 cm), with a stabilization of the H/L value,
617 suggesting that the flow erosivity cannot remove the entire thickness of the basal layer.
618 Figure 14 shows the results of the experiments and rock avalanche/flowslide data (Table S1) on the
619 same plot. Rock avalanches fall in the lowermost region of the graph. Data describing the nearly-
620 vertical collapse of large masses in the Yosemite valley (see Table S1, Wieczorek et al., 1999, Stock
621 and Uhrhammer, 2010) and chalk cliff collapses (Hutchinson, 2002; Duperret et al., 2006) exhibit a
622 much higher value of H/L. Data of our experiments falls in the region between these two data sets,
623 above the real large rock avalanches and to the left of vertical cliff collapses. At the same time, many
624 rock avalanche deposits of small to medium size show a behavior similar to that of the experiments.
625 We suggest a continuity in behavior and, despite the difference in scale, a similarity between these
626 different granular flows.
627 Figure 9a also shows the prediction of the simple model of Eq. 3. This model can explain the increase
628 in H/L with the slope, even though different parameters should be adopted for the three different
629 data sets. Real data can be fitted with relatively low friction coefficient and a coefficient of restitution
630 of the order 0.2-0.3. With such values, both data sets for rock avalanches and chalk flows are
631 approximately fitted by one single curve. This implies that the sharp increase in H/L for nearly vertical
632 collapses could be predicted by this simple analysis without invoking any anomalous behavior of the
633 chalk (Hutchinson, 2002). Experimental data, however, requires higher values of the friction
634 coefficient, like the one measured in the laboratory. In our model, the length L in the ratio H/L is
635 calculated as the sum of the horizontal slope on the inclined plate, plus the length on the horizontal

636 plate due to the residual horizontal velocity at the slope break. Our analysis with zero coefficient of
637 restitution is compatible with Okura's model (2000) for total loss of the vertical kinetic energy
638 component at the slope break.
639 The plot in Figure 9a also shows an empirical correlation between the length of the deposit at the
640 slope foot and the total length of the granular flow. Here, following a modified version of the $\alpha\beta$-
641 model by Lied and Bakkehøi (1980) for snow avalanches, we seek a correlation between the angle
642 of slope θ and the angle of Fahrboschung $\alpha = \tan^{-1}(H/L)$ in the form $\alpha = K\theta + B$, where K and B are
643 fitting constants. This empirical formula, shown in Fig. 9 with a dashed line ($H/L = \tan\alpha = 0.618\,\theta +$
644 9.8), appears to roughly fit our data. The fact that the fitting coefficients for the experiments are much
645 different from those pertinent to snow avalanches (0.77-0.94 instead of 0.618; Mc Clung, 2001) is
646 not surprising considering the complexity of snow avalanches in terms of wetting, cohesion, and air
647 entrainment. However, the analysis shows that the increase of H/L with slope angle has a common
648 origin. Comparison with the analysis by Lucas et al (2014) shows that we need a very large value of
649 the constant k to fit the H/L dataset, adopting their equation for Heim's ratio.
650 We note that the results of Fig. 9 could also be applicable to the well-known problem of the volume
651 effect, i.e., the decrease of the ratio H/L (Scheidegger, 1973) and of the effective friction coefficient
652 ($\mu_{eff} = \tan\theta + H_0/\Delta L$ where ΔL is the total runout measured along the real path; Lucas et al., 2014) as
653 a function of the volume for large rock avalanches. Although many theories have been put forward
654 to explain the volume effect (e.g., Legros, 2002, De Blasio, 2011a for short reviews; Lucas et al.,
655 2014), the fact that larger landslides will have lower impact angle θ shows that at least part of the
656 reason for the volume effect could be geometrical.

657

658 **5.2 Dynamics**

659 There are obvious differences between these sets of data. Our experimental flows are dry, while
660 chalk collapses occur in a wet environment; rock avalanches are mostly dry, but a collapse onto an
661 alluvial plain can lubricate their basal layers. Other experiments on an inclined granular bed, with no
662 sharp break in slope, have shown a gain rather than loss of mobility when the flume gradient is

steeper than approximately half the angle of repose of the material (Mangeney et al., 2010; Farin et al. 2014). This might be explained by the fact that the inclination causes an increase of the shear stress and a dry granular medium at slopes close to the angle of repose (or to critical friction angle; Crosta et al., 2015) is highly unstable. For wet materials close to saturation, the effect might be more dramatic with increased erosion and entrainment, and feedback effects leading in principle to unbounded growth of the flowing material (Breien et al., 2008; De Blasio et al., 2011; Iverson et al., 2011). Another difference is the effect of fragmentation of the granular mass, which is absent in the experiments given the fine grain size and low impact energy, but might alter the propagation of a real rock avalanche (McSaveney and Davies, 2007; Bowman et al., 2012) especially in correspondence to an abrupt break of slope (Crosta et al., 2007; De Blasio and Crosta, 2014, 2015). Considering these differences, the continuity between data and experimental flows is encouraging (Fig. 14).

Summarizing all the tests, a sequence of mechanisms occurring during the flow and deposition is suggested. As soon as the material impacts against the erodible substrate at the slope break, a sort of reflection controlled by the descent angle causes the ballistic/quasi ballistic projection of the material. The basal layer is dilated and eroded, and steeper deposit accumulates at the downstream side from which grains are launched ballistically. Where the ballistic trajectories meet the ground horizontal surface, a type of breaking wave is generated (Figs. 8b and 8c), which steepens during the earlier stages to become progressively gentler. During these stages, the flow and the wave erode material and transport it downstream causing a double (multiple) layering of the originally static material (tests with colored sand layers, Fig. 7).

Another interesting feature observed in the experiments for steep to very steep slopes (>45°) and in the numerical simulations (Crosta et al., 2015 and Fig. 5c) is the presence of a depression or groove left behind the deposit at the base of the inclined slope (for gentle slopes a backward propagating shock wave covers the slope toe and no depression is formed). Similar features have been described at the cliff foot for chalk falls (Hutchinson, 2002) or for snow avalanches from steep slopes (Corner, 1980; Smith et al., 1994, Fitzharris and Owens, 1984). Figure 10 shows a scheme of the morphology of snow-generated hollows. The impact pit geometry for snow avalanches (Smith et al., 1994; Owen

691 et al., 2006) suggests the role of impact force and erosion exerted by the highly energetic flow at
692 reshaping the slope toe. Both the truncated cone (B) and arcuate ridge (B) created by snow
693 avalanches in the natural setting resemble structures observed in the experiments and in the
694 simulations. We suggest that the depression observed in the numerical simulation at the slope break
695 is a good model for the pits observed in the field and in the experiments.

696 The upstream shock wave propagation is evident together with the infilling of the upstream
697 depression which initially isolates the crest of the deposit. This depositional process causes a
698 progressive upstream displacement of the center of mass at increasing the deposited volume.
699 Experiments using a coarse angular gravel (Figs. 6 and 8c) confirm the role of the flowing mass on
700 the erosion of the basal layer and the rapid mobilization of material with a type of ballistic motion. In
701 this case the eroded sand generates a wave running below the coarse gravel, which floats and finally
702 stops on the top of the sand deposit. Noticeably, the total runout, under the same experimental
703 conditions, is longer for the case of sand on sand experiments. All these observations suggest that
704 the thin layer approximation with minimal internal shear does not fit the evolution described here.
705 Dense shear flow conditions, the formation of ramp-like structures, the full detachment of the flow
706 front with formation of a breaking front are highly dynamic features.
707 As a further comparison with the field data we consider the Savage's number which gives the ratio
708 between inertial to gravity forces during the movement of the granular medium

709 $$N_{SAV} = D\frac{\dot{\gamma}^2}{g}$$

710 where D is the grain diameter and $\dot{\gamma}$ is the shear rate. Our experimental Savage's numbers
711 estimated during the collapse phase onto the horizontal board are typically of the order 10^{-2}, which
712 indicates a prevalence of gravity over inertia. The ratio between the Savage's number for the field
713 and the experiments can be recast in the form

714 $$\frac{N_{SAV}(field)}{N_{SAV}(exp)} = \frac{D(field)}{D(exp)}\frac{H(field)}{H(exp)}\left(\frac{T(exp)}{T(field)}\right)^2$$

715 where D, H, and T are respectively the grain size, the fall height, and the thickness of the shear layer.
716 Except for the fall height H (which is, however, extremely variable between different landslides), D

and T are poorly known and are also likely to vary enormously in the field. Using indicative ratios $\frac{D(field)}{D(exp)} = 1$ to 100; $\frac{H(field)}{H(exp)} = 1{,}000$; $\frac{T(exp)}{T(field)} = 1/100$ it is estimated that $\frac{N_{SAV}(field)}{N_{SAV}(exp)}$ may vary between 0.1 and 10. Thus, the experimental apparatus falls within the limit values of typical Savage's numbers occurring in nature.

All these observations suggest that the thin layer approximation with minimal internal shear does not fit the evolution described here, and multi layer models would be more realistic in the modeling of the real evolution. Dense shear flow conditions, the formation of ramp-like structures, the full detachment of the flow front with formation of a breaking front are highly dynamic features. This also supports the adoption of fully continuum or DEM models. Even if a simple elasto-plastic law does not allow an exact modelling of the entire phenomenon, it succeed at providing a qualitatively good geometrical fitting and especially at describing the internal deformation to which the material is subjected.

6. Conclusions

This paper presents the results of a series of physical and numerical experiments where a granular mass released along a slope reaches a horizontal plate with an abrupt slope change. If the horizontal plate is devoid of any granular material, the presence of a break of slope in the topography affects both dynamics and run-out. The geometry of the break of slope causes a loss of momentum perpendicular to the basal layer, with longer runout when the slope break is smoothed. Our observations substantiate and extend those made by Rowley et al. (2011) to a broader set of conditions (different slope angles and materials) by a detailed description of the evolution with time, and of the erosion mechanisms.

The main novelty of the present work, however, has been the study of the interaction of the granular flow descending along the slope with an erodible substrate of sand resting on the horizontal plate. To observe the dynamics of erosion and entrainment, the time evolution of the flow was monitored in detail. The modes of accretion and the final geometry of the deposit are found to be closely

744 associated with the slope angle and the momentum of the flow. In general, the presence of a dry
745 erodible substrate was found to hinder the further flow of the granular mass, but increase its volume.
746 Thus, the experiments suggest that in a real landslide, a granular flow falling at a steep angle onto
747 a loose, dry erodible substrate will decrease its speed and run-out. The physical reason for this lays
748 in the transfer of momentum to the erodible substrate.
749 A series of analytical and numerical models are presented to simulate experimental tests A solution
750 for the H/L ratio which contains the effect of the abrupt slope break and a coefficient of restitution is
751 presented and the obtained relationship fits well both the experiments and the real case data.
752 Numerical simulations via a FEM ALE approach, adopting an elasto-plastic Mohr Coulomb material
753 description, confirm the direct increase on the run-out when the slope break is smoothed. The
754 dynamics of flow, erosion and entrainment simulated numerically support the observation of a dense
755 flow condition especially during the propagation along the horizontal portion and the internal shearing
756 till the final deposition. The numerical results reproduce well the dynamics observed, peak velocity
757 and total duration, including the dense shear flow erosion of the basal layer and the geometry of the
758 final deposit. Starting from recent modeling literature, the adoption of a $\mu(I)$ frictional rheology is
759 suggested for modeling this type of processes. Future efforts will test a visco-plastic approach on
760 the same set of data and constraints.
761

762 **Acknowledgements**

763 The data for this paper are available upon request from the authors. The research was supported
764 by PRIN Project: Time - Space prediction of high impact Landslides under changing precipitation
765 regimes PRIN 2010–2011 — prot. 2010E89BPY_007 project by the Italian Ministry of Research and
766 University. Jeff Warburton is thanked for the critical reviewing of an early version of the manuscript.
767

768 **References**

769

770 ASTM D3080 / D3080M-11, Standard Test Method for Direct Shear Test of Soils Under Consolidated
771 Drained Conditions, ASTM International, West Conshohocken, PA, 2011, www.astm.org

772 ASTM D7263-09, Standard Test Methods for Laboratory Determination of Density (Unit Weight) of
773 Soil Specimens, ASTM International, West Conshohocken, PA, 2009, www.astm.org
774 Bowman, E.T., Take, W.A., Rait, K.L., Hann, C. (2012) Physical models of rock avalanche spreading
775 behaviour with dynamic fragmentation Can. Geotech. J. 49: 460–476 (2012)
776 Breien, H., De Blasio, F.Ellverhoi, A., and Hoeg, K. (2008). Erosion and morphology of a debris flow
777 caused by a glacial lake outburst flood. Landslides. DOI: 10.1007/s10346-008-0118-3.
778 Calvetti, F., Crosta, G., Tatarella, M. (2000) Numerical simulation of dry granular flows: from the
779 reproduction of small-scale experiments to the prediction of rock avalanches. Rivista Italiana di
780 Geotecnica 34(2), 21–38.
781 Chen, H., Crosta, G. B., Lee C.F. (2006) Erosional effects on runout of fast landslides, debris flows
782 and avalanches: a numerical investigation. Geotechnique, 56, 5, 305–322.
783 Choffat, P. (1929), L'ecroulement d'Arvel (Villeneuve) de 1922, Bull. Soc. Vaudoise Sci. Nat., 57(1),
784 5 – 28.
785 Corner, G. D. (1980) Avalanche impact landforms in Troms, north Norway. Geografiska Annaler,
786 62A: 1-10
787 Crosta, G. B., Imposimato, S., Roddeman, D., Chiesa, S., Moia, F. (2005), Small fast moving flow-
788 like landslides in volcanic deposits: The 2001 Las Colinas Landslide (El Salvador), Engineering
789 Geology 79(3– 4), 185–214, doi:10.1016/j.enggeo.2005.01.014.
790 Crosta G.B., S. Imposimato, D.G. Roddeman (2006) Continuum numerical modelling of flow-like
791 landslides. Landslides from massive rock slope failure, Evans, S.G., Scarascia Mugnozza, G.,
792 Strom, A., Hermanns, R., (eds) NATO Science Series, Earth and Environmental Sciences, 49,
793 211-232
794 Crosta, G. B., Frattini, P., Fusi. N. (2007), Fragmentation in the Val Pola rock avalanche, Italian Alps.
795 J. Geophys Res., 112, F01006, doi:10.1029/2005JF000455.
796 Crosta, G. B., Imposimato, S., Roddeman, D. (2008) Numerical modelling of entrainment/deposition
797 in rock and debris-avalanches. Engineering Geology, 109, 1-2, 135-145.
798 Crosta, G. B., Imposimato, S., Roddeman, D. (2009) Numerical modeling of 2-D granular step
799 collapse on erodible and non erodible surface. J. Geophys. Res., 114, F03020.

800 Crosta, G. B., Imposimato, S., Roddeman, D. (2015b). Landslide Spreading, Impulse Water Waves
801 and Modelling of the Vajont Rockslide. Rock Mechanics and Rock Engineering, 10.1007/s00603-
802 015-0769-z, 1-24.
803 Crosta, G.B., Imposimato, S., Roddeman, D. (2013a) Interaction of Landslide Mass and Water
804 Resulting in Impulse Waves. In Landslide Science and Practice, Vol. 5: Complex Environment.
805 Margottini, C., Canuti, P., Sassa, K. (Eds), ISBN 978-3-642-31426-1,28 DOI 10.1007/978-3-642-
806 31427-8, Springer, 49-56
807 Crosta, G.B., Imposimato, S., and Roddeman, D. (2015a). Granular flows on erodible and non
808 erodible inclines. Granular Matter, DOI 10.1007/s10035-015-0587-8.
809 Crosta, G.B., Imposimato, S., Roddeman, D., Frattini, P. (2013b) On Controls of Flow-Like Landslide
810 Evolution by an Erodible Layer. In Landslide Science and Practice, Vol. 3: Spatial Analysis and
811 Modelling. Margottini, C., Canuti, P., Sassa, K. (Eds), ISBN 978-3-642-31426-1,28 DOI
812 10.1007/978-3-642-31427-8, Springer, 263-270
813 Cruden, D.M., Hungr, O. (1986) The debris of Frank slide and theories of rockslide-avalanche
814 mobility. Canadian Journal of Earth Sciences, 23, 425-432.
815 De Blasio, F.V. (2011) Landslides in Valles Marineris (Mars): a possible role of basal lubrication by
816 sub-surface ice. Planetary and Space Science 59, 1384-1392. doi: 10.1016/j.pss.2011.04.015.
817 De Blasio, F.V., and Crosta, G.B. (2014). Simple physical model for the fragmentation of rock
818 avalanches. Acta Mechanica, DOI 10.1007/s00707-013-0942-y.
819 De Blasio, F.V., Breien, H., Elverhøi, E. (2011). Modelling a cohesive-frictional debris flow: an
820 experimental, theoretical, and field-based study. Earth Surface Processes and Landforms 36,
821 753–766.
822 Denlinger, R. P., Iverson, R. M. (2001), Flow of variably fluidized granular masses across three-
823 dimensional terrain: 2. Numerical predictions and experimental tests, J. Geophys. Res., 106(B1),
824 553 – 566, doi:10.1029/2000JB900330.

825 Dufresne, A. (2012) Granular flow experiments on the interaction with stationary runout path
826 materials and comparison to rock avalanche events. Earth Surf. Processes Landforms, 37, 1527-
827 1541
828 Duperret, A., Genter, A., Martinez, A., Mortimore, R.N. (2006) Coastal chalk cliff instability in NW
829 France: role of lithology, fracture pattern and rainfall. In Mortimore, R. N. and Duperret, A. (eds),
830 Coastal Chalk Cliff Instability. Geological Society, London, Engineering Geology Special
831 Publications, The Geological Society of London 20, 33-55.
832 Erismann, T. H., Abele, G. (2001) Dynamics of Rockslides and Rockfalls. Springer-Verlag, Berlin,
833 316 pp.
834 Farin, M., Mangeney, A., Roche, O. (2014) Fundamental changes of granular flow dynamics,
835 deposition and erosion processes at high slope angles: insights from
836 laboratory experiments. Journal of Geophysical Research-Earth Surface, 119: 504-532,
837 doi:10.1002/2013JF002750.
838 Fitzharris, B. B., Owens, I. F. (1984) Avalanche tarns. Journal of Glaciology, 30(106): 308-312.
839 Forterre, Y., Pouliquen, O. (2008) Flows of dense granular media, Annu. Rev. Fluid Mech., 40, 1–
840 24.
841 Gray, J. M.N.T. Wieland, M., Hutter K. (1999) Gravity-driven free surface flow of granular avalanches
842 over complex basal topography. Proc. R. Soc. Lond., A, 455, doi: 10.1098/rspa.1999.0383
843 Hakonardottir, K. M., Hogg, A. J., Johannesson, T., Kern, M., Tiefenbacher, F. (2003a) Large scale
844 avalanche braking mound and catching dam experiments with snow. A study of the airborne jet.
845 Surveys in Geophysics, 24, 543–554.
846 Hakonardottir, K. M., Hogg, A. J., Johannesson, T., Tomasson, G.G. (2003b) A laboratory study of
847 the retarding effects of braking mounds on snow avalanches. Journal Glac., 49(165), 191–200.
848 Heim, A. (1882). Der Bergsturz von Elm: Deutsch.Geol. Gesell. Zeitschr. 34, 74-115Heim, A. (1932)
849 Bergsturz und Menchenleben. Fretz und Wasmuth, Zürich, 1-218.
850 Hewitt, K. (2006) Rock avalanches with complex run out and emplacement, Karakoram Himalaya,
851 Inner Asia. S.G. Evans et al. (eds.), Landslides from Massive Rock Slope Failure, Springer. Printed
852 in the Netherlands 521–550.

853 Hsu, K. (1975) Catastrophic Debris Streams (Sturzstroms) Generated by Rockfalls. Geological
854 Society of America Bulletin, 86, 129-140.
855 Hutchinson, J.N. (2002) Chalk flows from the coastal cliffs of northwest Europe. Geological Society
856 of America, Reviews in Engineering Geology, 2002, 15, 257-302
857 Iverson, R. M. (2012) Elementary theory of bed-sediment entrainment by debris flows and
858 avalanches. Journal of Geophysical Research: Earth Surface (2003–2012), 117(F3)
859 Iverson, R. M., and C. Ouyang (2015), Entrainment of bed material by Earth-surface mass flows:
860 Review and reformulation of depth-integrated theory, Rev. Geophys., 53, doi:10.1002/
861 2013RG000447.
862 Iverson, R.M., Reid, M.E., Logan, M., LaHusen, R.G., Godt, J.W., Griswold, J.G. (2011) Positive
863 feedback and momentum growth during debris-flow entrainment of wet bed sediment. Nature
864 Geoscience 4:116-121. doi: 110.1038/NGEO1040.
865 Jaboyedoff, M. (2003) The rockslide of Arvel caused by human activity (Villeneuve, Switzerland):
866 Summary, partial reinterpretation and comments of the work of Ph. Choffat (1929): L'ecroulement
867 d'Arvel (Villeneuve) de 1922. Bull. SVSN 57, 5 – 28, Open File Rep. 3, Int. Indep. Cent. of Clim.
868 Change Impact on Nat. Risk Anal. in Mt. Areas, Lausanne, Switzerland. (Available at
869 http://www.quanterra.org/erosion hazard.htm.)
870 Lacaze, L., Phillips, J. C., Kerswell, R. R. (2008) Planar collapse of a granular column: Experiments
871 and discrete element simulations, Phys. Fluids, 20, 063302.1–063302.12, doi:10.1063/1.2929375.
872 Lajeunesse, E., Mangeney-Castelnau, A., Vilotte, J. P. (2004) Spreading of a granular mass on a
873 horizontal plane, Phys. Fluids, 16, 2371–2381, doi:10.1063/1.1736611.
874 Lajeunesse, E., Monnier, J. B., Homsy, G. M. (2005) Granular slumping on a horizontal surface,
875 Phys. Fluids, 17, 103302.1 – 103302.15, doi:10.1063/1.2087687.
876 Legros, F. (2002) The mobility of long-runout landslides, Engineering Geology, 63, 301-331.
877 Lied, K., Bakkehøi, S. (1980) Empirical calculations of snow-avalanche run-out distance based on
878 topographic parameters. J. Glac. 26, 165-177.

879 Lube, G., Huppert, H., Sparks, S., Freundt, A. (2005) Collapses of two dimensional granular
880 columns. Phys. Rev. E, 72, 041301.1–041301.10, doi:10.1103/PhysRevE.72.041301.
881 Lucchitta, B. K. (1979) Landslides in Valles Marineris, Mars, J. Geophys. Res., 84(B14), 8097–8113,
882 doi:10.1029/JB084iB14p08097.
883 Ma, A., Liao, H., Ning, C., Feng, Z. (2014) Stability analysis of a high slope along a loess plateau
884 based on field investigation and numerical analysis. K. Sassa et al., (eds), Landslide Science for
885 a safer Geoenvironment, Springer, vol. 1, 451-458
886 Mangeney, A., Roche, O., Hungr, O., Mangold, N., Faccanoni, G., Lucas A. (2010) Erosion and
887 mobility in granular collapse over sloping beds, J. Geophys. Res.- Earth Surface, 115, F03040.
888 Mangeney, A., Tsimring, L.S., Volfson, D., Aranson, I.S., Bouchut, B. (2007) Avalanche mobility
889 induced by the presence of an erodible bed and associated entrainment, Geophys. Res. Lett., 34,
890 L22401,
891 Manzella, I., Labiouse, V. (2008) Qualitative analysis of rock avalanches propagation by means of
892 physical modelling of not constrained gravel flows. Rock Mechanics and Rock Engineering, 41
893 (1), 133–151
894 Manzella, I., Labiouse, V. (2013) Empirical and analytical analyses of laboratory granular flows to
895 investigate rock avalanche propagation. Landslides (2013) 10:23–36, DOI 10.1007/s10346-011-
896 0313-5
897 McClung, D.M. (2001) Extreme avalanche runout: a comparison of empirical models. Can. Geotech.
898 J. 38: 1254–1265, DOI: 10.1139/cgj-38-6-1254
899 McConnell, R.G., Brock, R.W. (1904) Report on great landslide at Frank, Alberta, Canada. Can. Dep.
900 Inter., Annu. Rep., 1902—1903, Part 8, 17 pp.
901 McDougall, S. (2006) A new continuum dynamic model for the analysis of extremely rapid landslide
902 motion across complex 3D terrain. PhD thesis, Univ British Columbia, 253 pp.
903 McSaveney, M.J., Davies, T. (2007) Rockslides and their motion. In Sassa K., Fukuoka F., Wang F.,
904 Wang G. (eds), Progress in landslide science, Springer, Berlin, 113-133

McSaveney, M.J., Davies, T.R.H., Hodgson, K.A. (2000) A contrast in deposit style and process between large and small rock avalanches. In: Bromhead E, Dixon D, Ibsen M–L (eds) Landslides in research, theory and practice. Thomas Telford Publishing, London, pp 1053–1058

Okura, Y., Kitahara, H., Kawanami, A., Kurokawa, U. (2003) Topography and volume effects on travel distance of surface failure. Eng. Geol. 67, 243-254.

Okura, Y., Kitahara, H., Sammori, T., Kawanami, A. (2000). The effects of rockfall volume on runout distance. Engineering Geology, 58(2), 109-124

Owen, G., Matthews, J. A., Shakesby, R. A., He, X. (2006) Snow-avalanche impact landforms, deposits and effects at Urdvatnet, southern Norway: implications for avalanche style and process. Geografiska Annaler: Series A, Physical Geography, 88: 295–307. doi: 10.1111/j.0435-3676.2006.00302.x

Pastor M, Blanc T, Pastor MJ (2009) A depth-integrated viscoplastic model for dilatant saturated cohesive-frictional fluidized mixtures: application to fast catastrophic landslides. J. Non-Newtonian Fluid Mech., 158:142–153

Pastor, M., Blanc, T., Haddad, B., Petrone, S., Morles, M. S., Drempetic, V., Issler, D., Crosta, G.B., Cascini, L., Sorbino, G., Cuomo, S. (2014). Application of a SPH depth-integrated model to landslide run-out analysis. Landslides, 1-20, 10.1007/s10346-014-0484-y

Pudasaini, S., Kroner, C. (2008) Shock waves in rapid flows of dense granular materials: Theoretical predictions and experimental results. Phys. Rev. E 78, 041308.

Pudasaini, S.P., Hutter, K. (2006) Avalanche Dynamics: Dynamics of Rapid Flows of Dense Granular Avalanches, ISBN: 3-540-32686-3, Springer-Verlag, 602 pp.

Roddeman, D.G. (2008) TOCHNOG user's manual. FEAT, 255 pp, www.feat.nl/manuals/user/user.html.

Rowley, P.J, Kokelaar, P., Menzies, M., Waltham, D. (2011) Shear-derived mixing in dense granular flows. Journal of Sedimentary Research 81:974-884, doi: 910.2110/jsr.2011.2172.

930 Scheidegger, A.E. (1973) On the prediction of the reach and velocity of catastrophic landslides. Rock
931 Mechanics 5, 231-236.
932 Smith, D.J. McCarthy, D.P., Luckman, B.H. (1994) Snow-Avalanche Impact Pools in the Canadian
933 Rocky Mountains Arctic and Alpine Research, Vol. 26, No. 2, 1994, pp. 116-127
934 Staron, L. (2008). Mobility of long-runout rock flows: a discrete numerical investigation. Geophysical
935 Journal International, 172(1), 455-463.
936 Stock, G. M.,Uhrhammer, R. A. (2010) Catastrophic rock avalanche 3600 years BP from El Capitan,
937 Yosemite Valley, California. Earth Surf. Process. Landforms, 35: 941–951. doi: 10.1002/esp.1982
938 Strom, A. (2006) Morphology and internal structure of rockslides and rock avalanches: grounds and
939 constraints for their modelling. S.G. Evans et al. (eds.), Landslides from Massive Rock Slope
940 Failure, Springer, 305–326.
941 Taboada, A., Estrada, N. (2009). Rock-and-soil avalanches: Theory and simulation. Journal of
942 Geophysical Research: Earth Surface (2003–2012),114(F3).
943 Utili, S., Zhao, T., Houlsby, G.T. (2015) 3D DEM investigation of granular column collapse:
944 Evaluation of debris motion and its destructive power. Engineering Geology, 186, 3-16
945 von Poschinger, A., Kippel, Th. (2009) Alluvial deposits liquefied by the Flims rock slide. Engineering
946 Geology, Vol. 103, 1, 50-56.
947 Wieczorek, G.F., Morrissey, M.M., Iovine, G., Godt, J. (1999) Rock-fall potential in the Yosemite
948 Valley, California. US Geological Survey Open-file Report 99–578.
949 Zhao, T., Utili, S., Crosta, G. B. (2015) Rockslide and Impulse Wave Modelling in the Vajont
950 Reservoir by DEM-CFD Analyses. Rock Mechanics and Rock Engineering, 1-20.
951
952
953

954 **FIGURE**

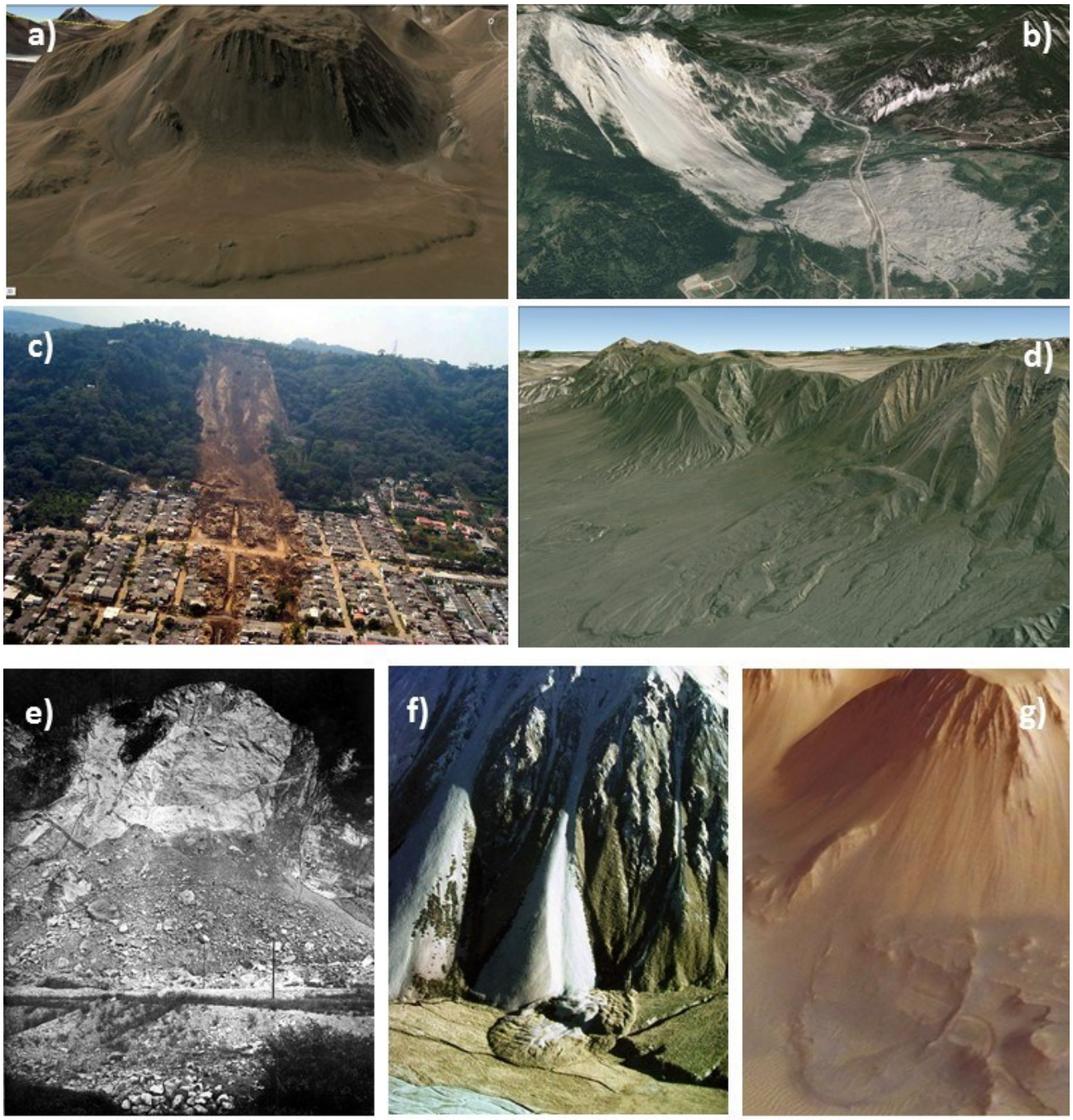

955

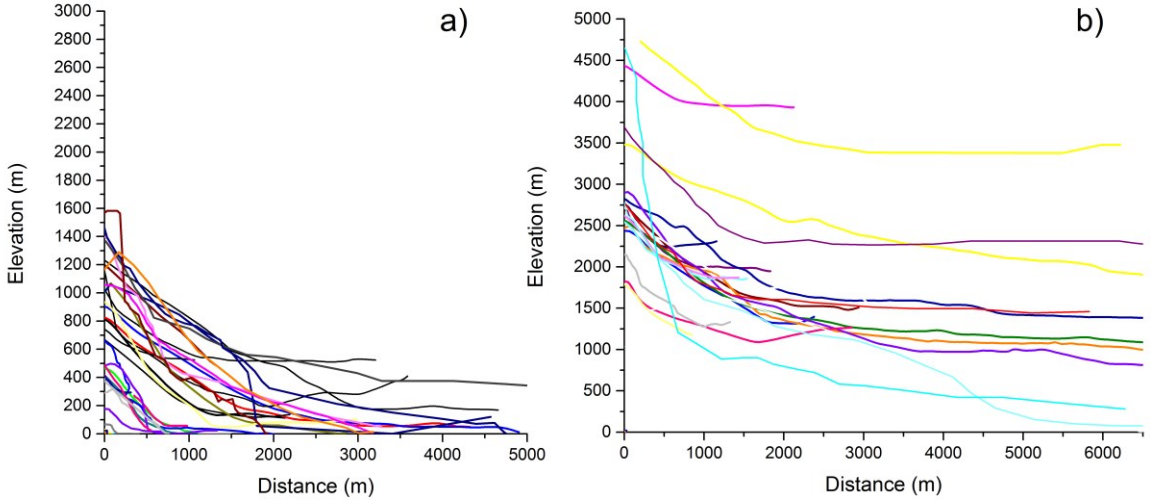

956

957

958 *Figure. 1 Example of rock avalanches along simple break of slope profiles and possible interaction*
959 *with the material at the base of the accumulation. a) rock avalanche in Northern Chile (Crosta et al.,*
960 *2013) (GoogleEarth™); b) Frank slide, Alberta, Canada (Cruden and Hungr, 1986) (GoogleEarth™);*
961 *c) Las Colinas flowslide (San Salvador; Crosta et al., 2005; http://landslides.usgs.gov/research/*
962 *other/images); d) Central Tien Shan (Strom, 2006), rock avalanche in Paleozoic granite (ca 300*10^6*
963 *m^3) (GoogleEarth™); e) Arvel rock fall-avalanche (Choffat, 1929); f) South Ashburton rockslide, New*
964 *Zealand (McSaveney et al. 2000); g) Mars, Noctis Labyrinthus(GoogleEarth™). See also Table 1S*
965 *in supplementary material for geometrical details; a series of typical rock avalanche slope*
966 *profiles, characterized by a bilinear-like geometry is shown in fig. 1h and 1i.*

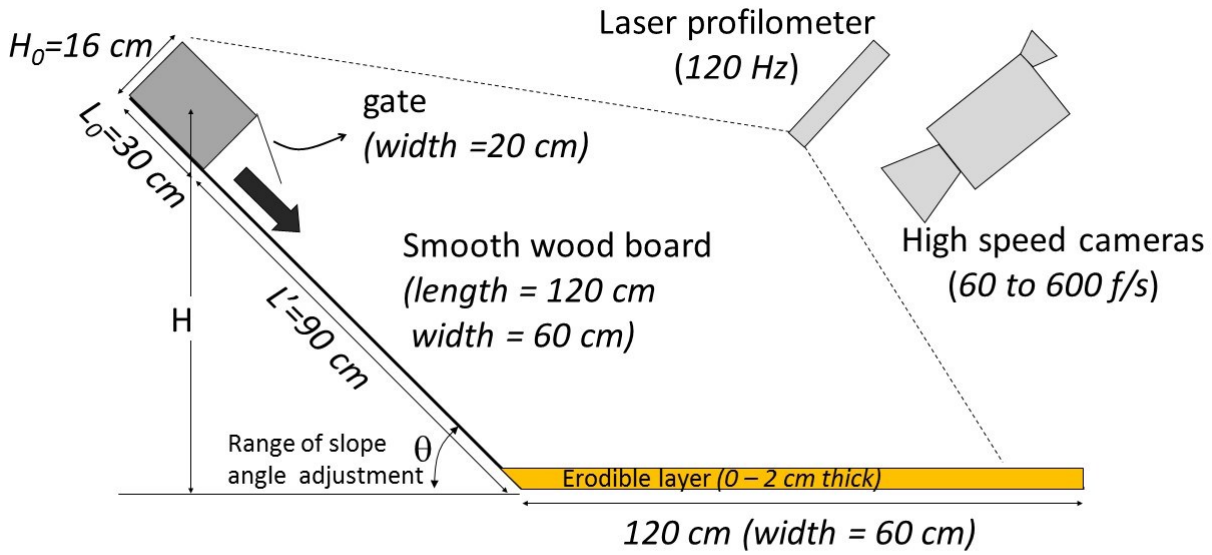

967

968 *Figure 2 Sketch of the experimental setup. The time evolution of the flow and the propagation of*
969 *the front position are observed by sampling the centerline profile at 120 Hz, and by two high-speed*
970 *cameras.*

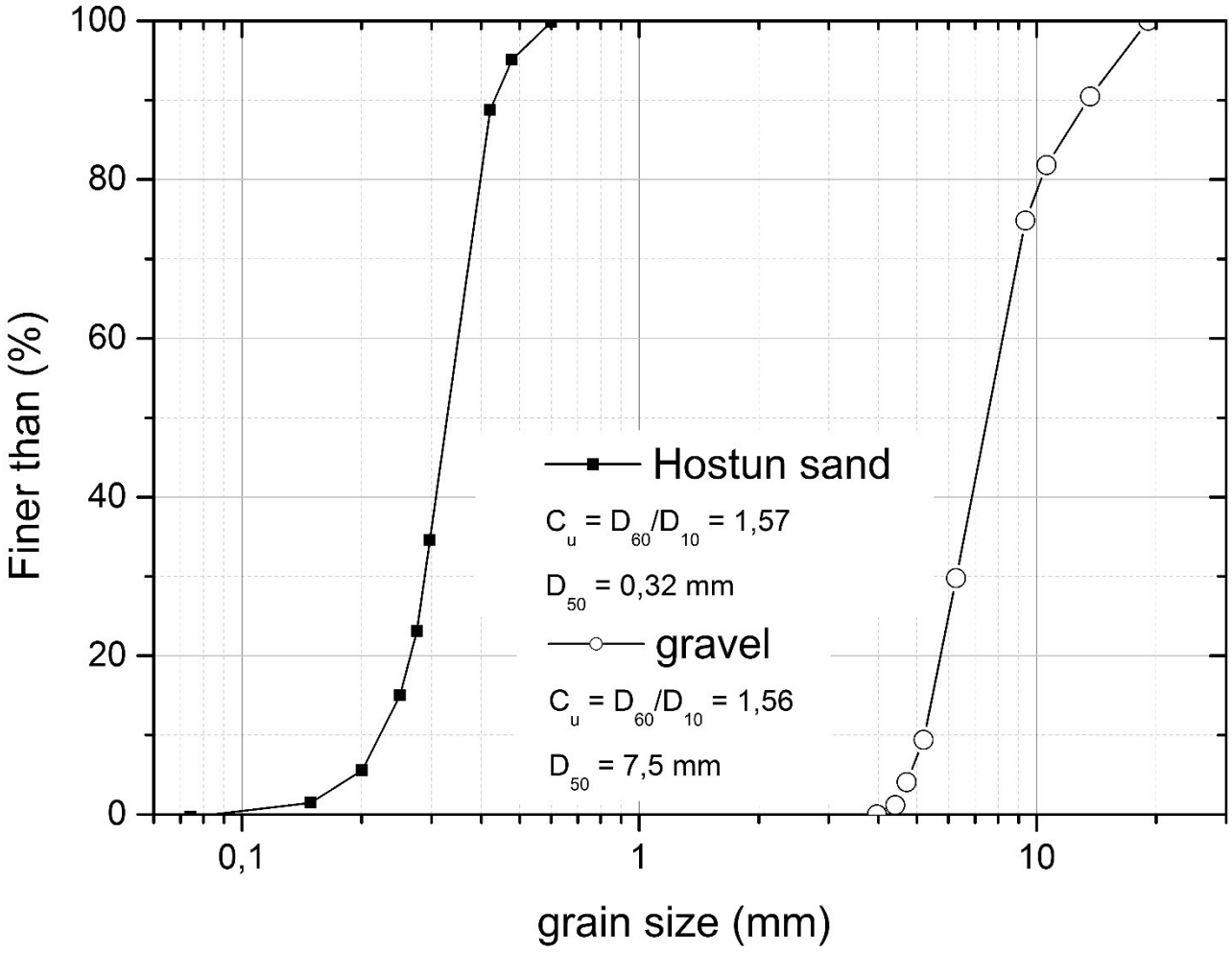

971

972 *Figure 3 Grain size curves for the Hostun silica sand and the angular gravel used in the tests.*

973 *Uniformity coefficient and D_{50} values are also reported.*

974

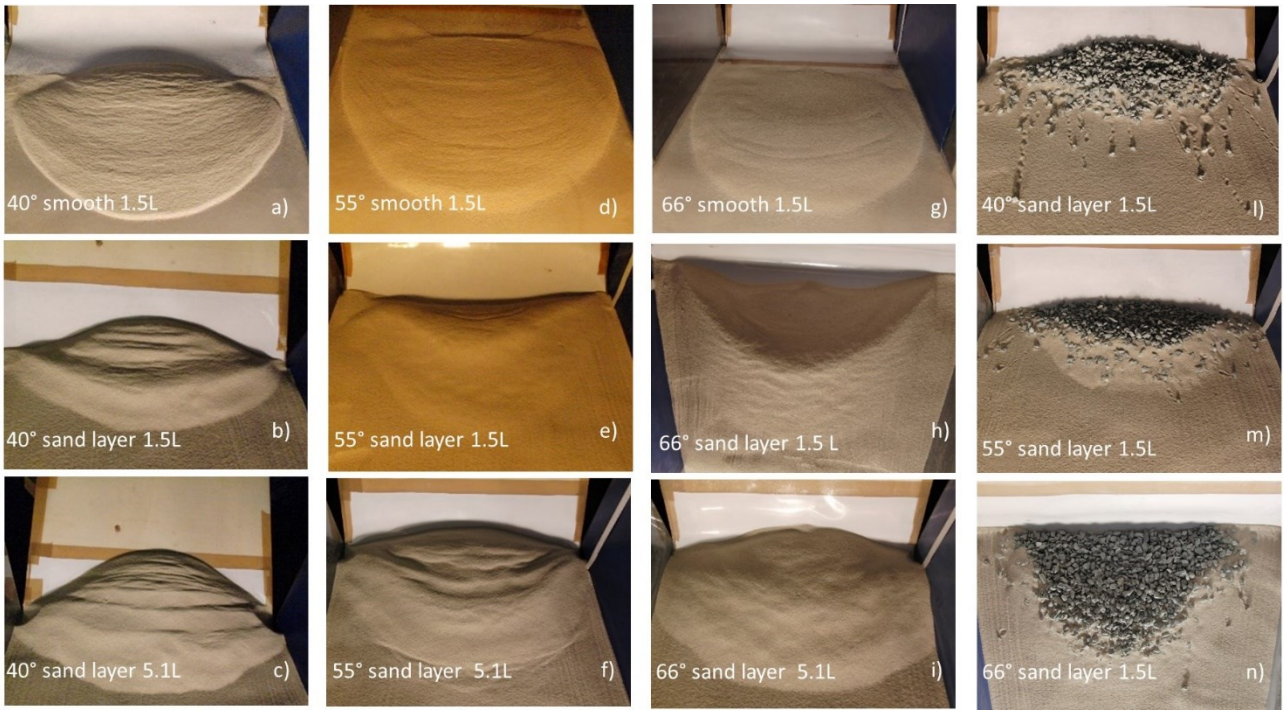

Figure 4 Examples of different deposit characteristics observed for tests release of different volumes (1.5 L to 5.1 L) at changing slope inclination (40°, 55°, 66°), on a smooth surface or on a basal sandy layer. a-f: tests with sand; l-n: tests with gravel on sand.

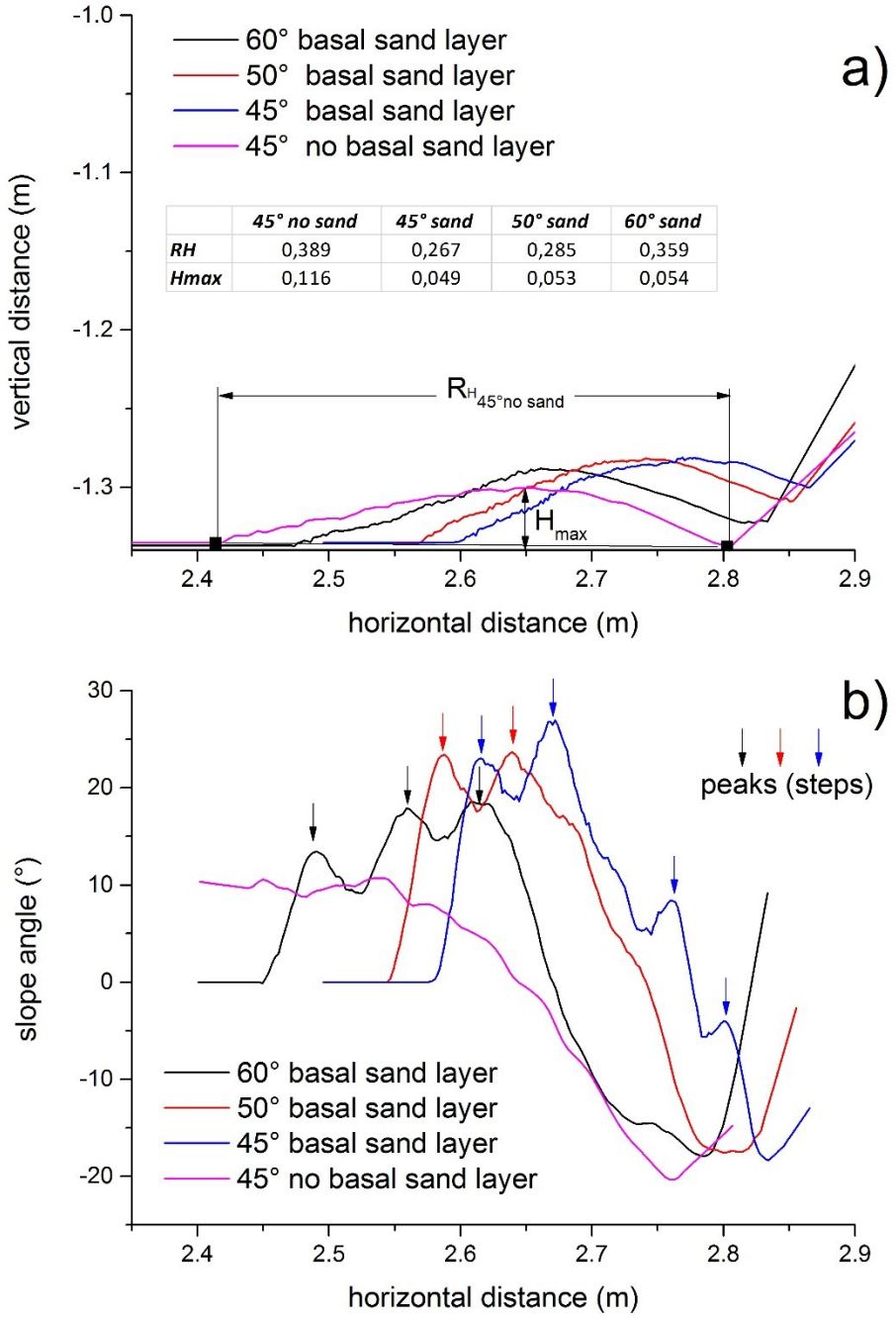

	45° no sand	45° sand	50° sand	60° sand
RH	0,389	0,267	0,285	0,359
Hmax	0,116	0,049	0,053	0,054

Figure 5 Comparison of final deposit morphologies at varying slope angle (45° to 60°) and with or without the basal sand layer. Test material: Hostun sand. a) deposit profiles as surveyed along the centerline with the axis origin at the position of the laser acquisition system. The inset table shows the values of maximum deposit length (L) and maximum thickness (H_{max}); b) slope angle computed on a 10 points smoothing window. Arrows evidence the peaks in the slope angles which can be associated to internal deformations and backward propagation of the deposit.

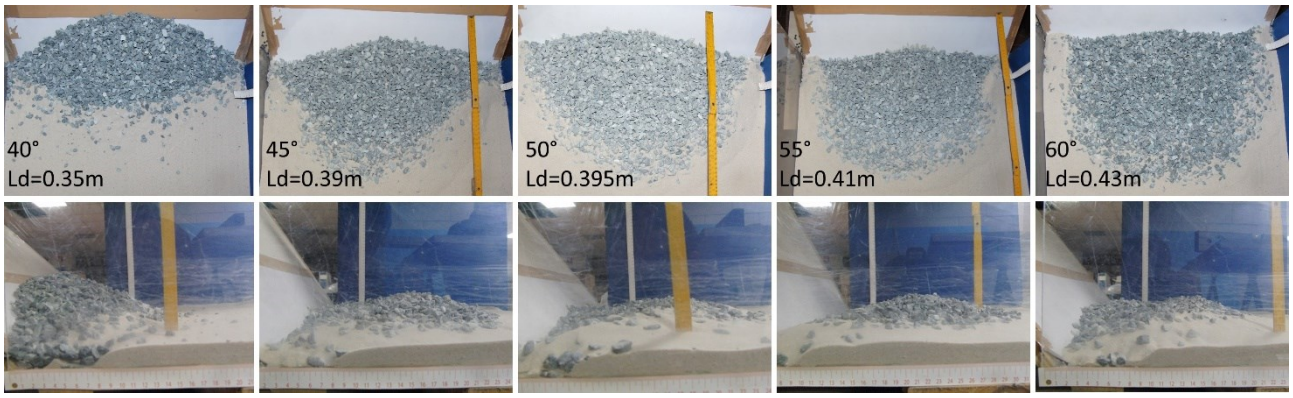

Figure 6 Final geometry of the deposit of gravel above the basal sandy layer at increasing slope angle and for constant release volume. Particles outrunning the main deposit are visible at low slope angles whereas a wedge of disturbed sand appears in the front of the deposit. R_H in the figures represents the length of the deposit.

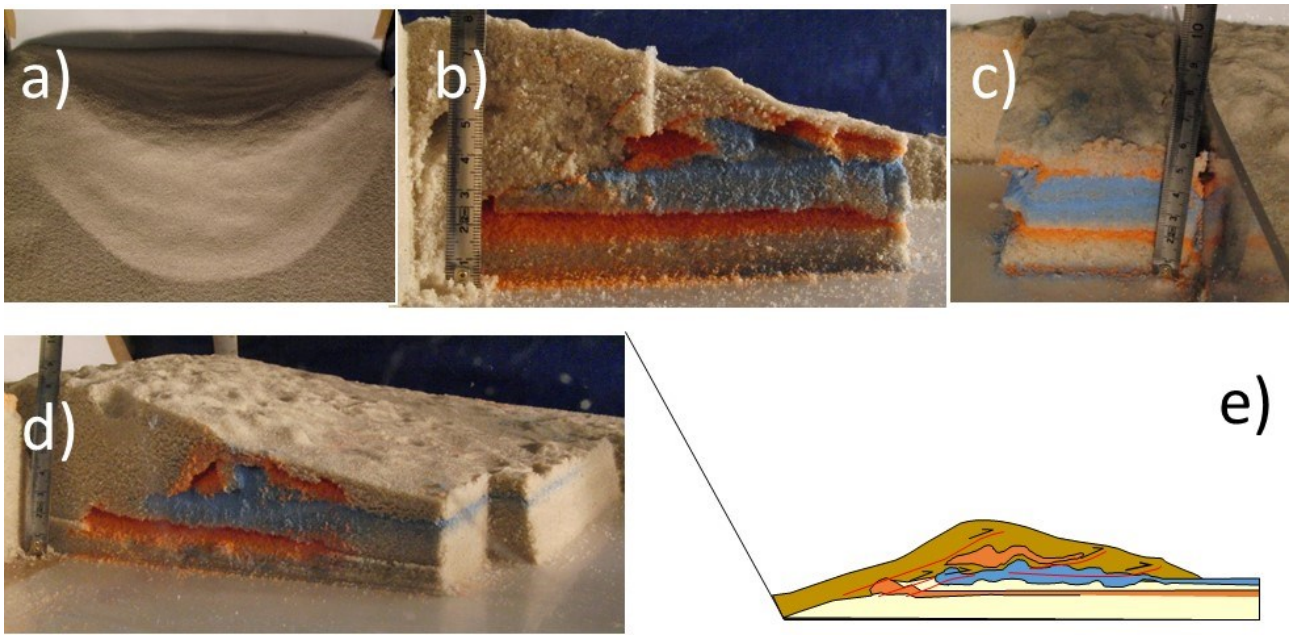

Figure 7. Internal structures and kinematic interpretation of the erosion and deposition from the result of tests with colored sand layers. a) bird's view of the deposit for an experiment with a 66° slope and 5.1 litres release volume*; b)-d): longitudinal and transversal sections and view of the deposit. Doubling of the orange layer and thickening of the upper blue layer due to erosion and transport (left to right in b) and d)) is visible. The main low angle shearing and erosion plane is seen in b) by the sharp contact between the uncolored Hostun sand and the colored layers. A simplified description*

999 *of the general geometry of the layers is shown in e) where the brownish / mustard tone is used for*
1000 *the granular flow deposit.*

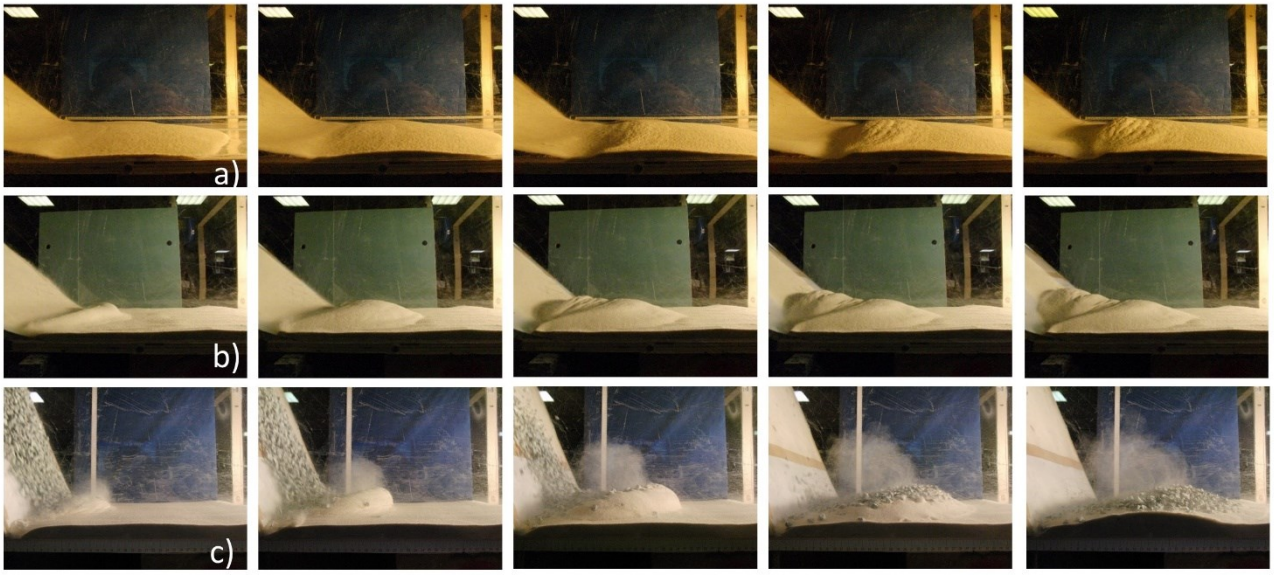

1001

1002 *Figure 8a. Time-lapse sequence of photos showing the evolution of the granular flow for a) a Hostun*
1003 *sand mass flowing on a 40° slope, from the impact on the smooth (rigid) horizontal board to final*
1004 *deposition; b) for a Hostun sandy mass flowing on a 40° slope and c) a gravelly mass flowing on a*
1005 *66° slope, both from the impact on the basal layer of the Hostun sand to final deposition. Time runs*
1006 *from left to right and top to bottom images. Time interval: 0.096 s.*

1007

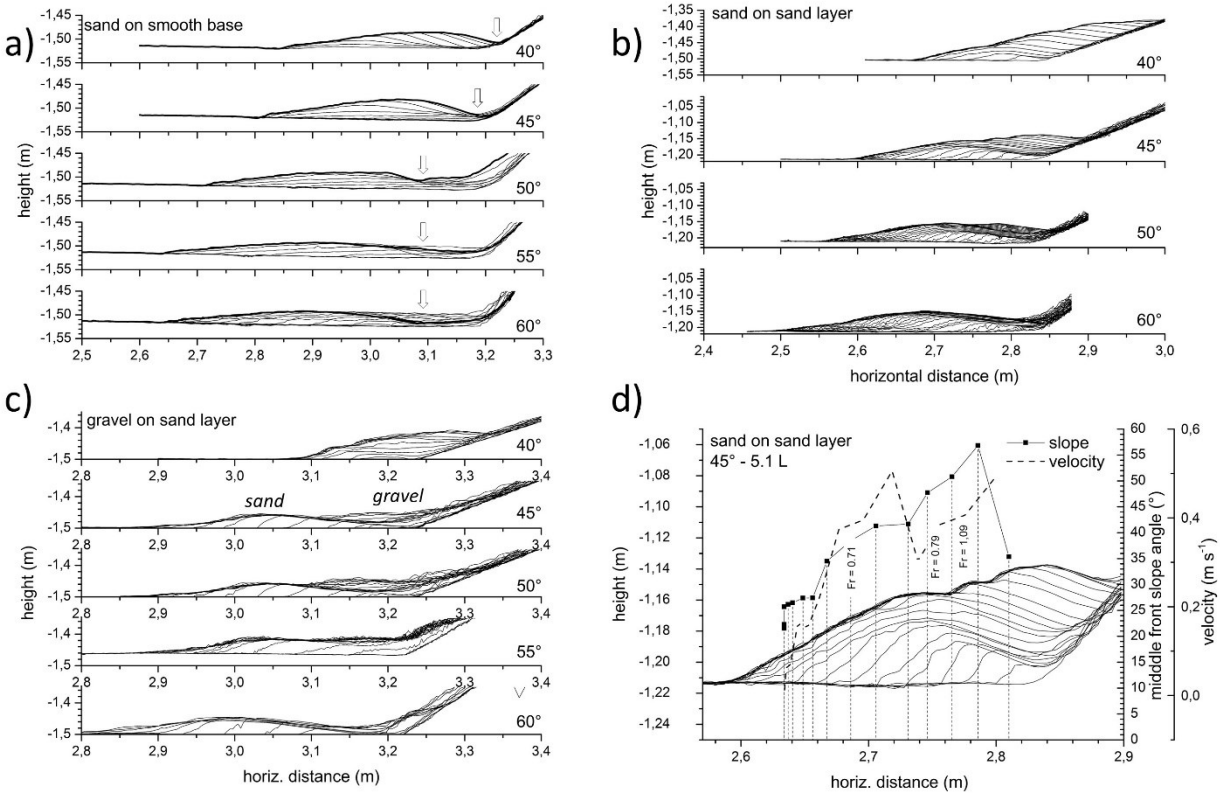

Figure 9. Evolution of profiles of the flowing mass for different times and different experimental conditions. Each profile portrays the sand distribution every 0.02 s. a) sand on a smooth base; arrows indicate the farthest point reached by the last grains. b) sand on basal sand layer; c) gravel on basal sand layer; d) enlargement of profiles from b) for a 45° slope, with computed front slope angle and velocity. Froude number is shown at three different points.

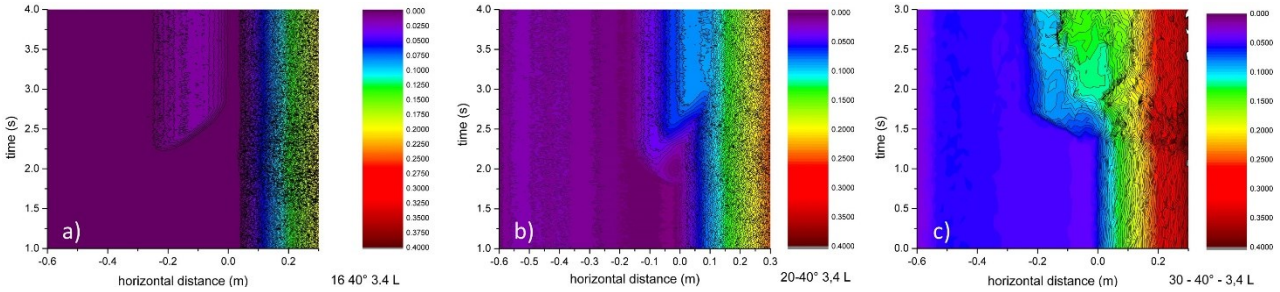

Figure 10. a) Space-time plots showing the evolution with time of the flow profile (z value) along the flow/deposit centerline for a) a sand mass on smooth surface, b) a sand mass on an erodible sand layer, c) a gravel mass on an erodible sand layer. All the tests are performed releasing 3.4 litres of material on a 40° slope. Frequency of acquisition: 120 Hz. Contour interval: 0.005 m. The values

1019 *reported in the graphs (e.g. 16 40˚ 3.4L) refer to the test number, the slope inclination and the release*
1020 *volume. More results are presented in the Supplementary material (Figs. S1 a, b, and c).*
1021

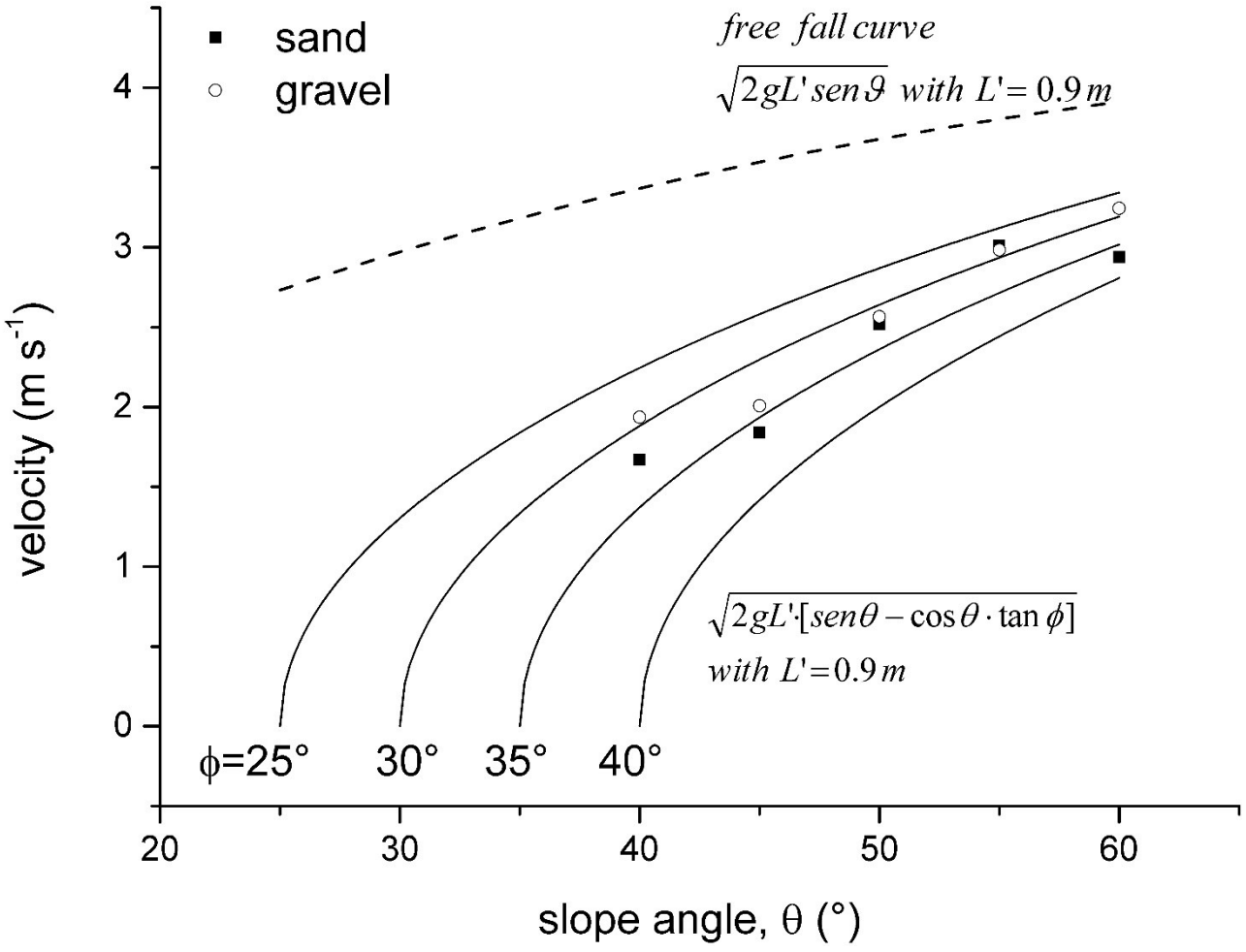

1022

1023 *Figure 11. Final velocity at the end of the sloping board for sand and gravel as derived from*
1024 *monitored profiles, compared with theoretical results for free fall and fall along the slope at constant*
1025 *path length (L'=0.9m) and changing slope angle (θ), and for variable friction angles*
1026 *($\sqrt{2\ gL'(sen\theta-cos\theta\ tan\varphi)}$).*

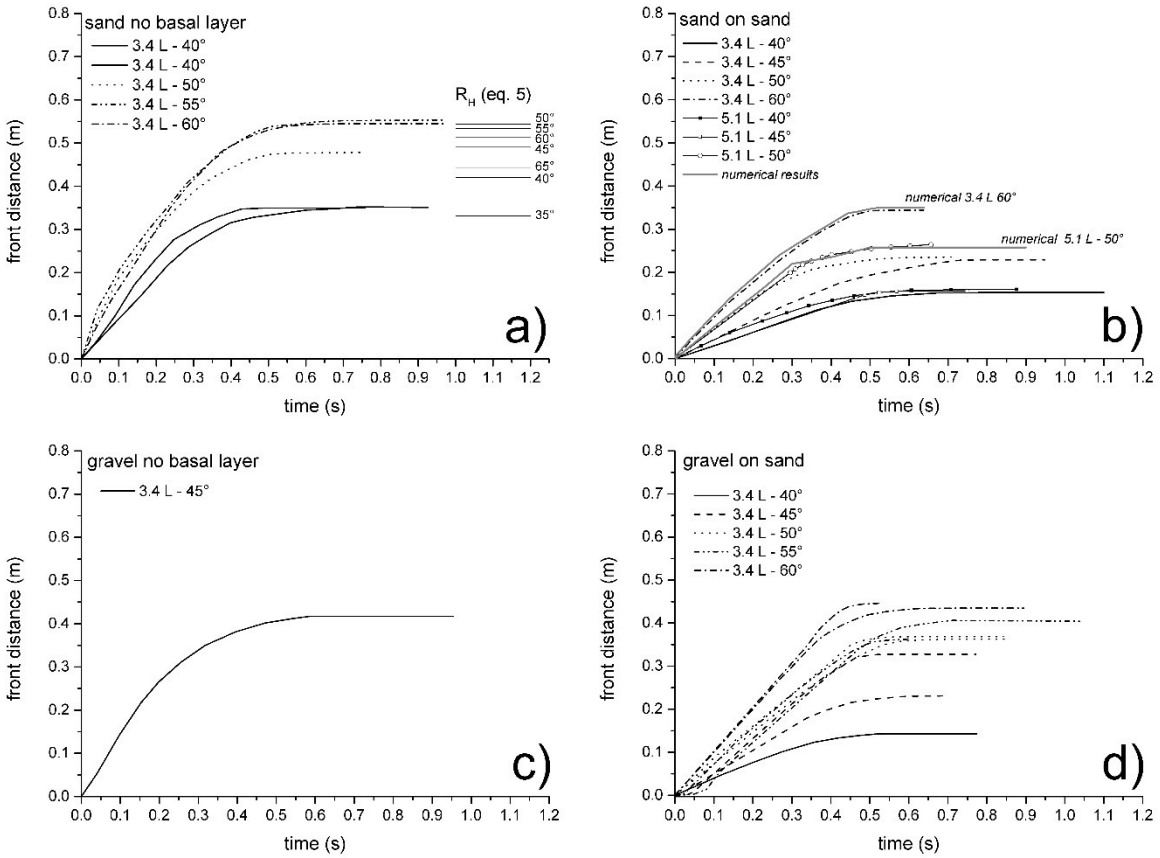

Figure 12. Front position, along the horizontal sector of the path, versus time plots for different test conditions (volume: 3.4 and 5.1 l). a) sand on smooth surface, with comparison of results by applying Eq. 5 for calculation of maximum runout on the horizontal sector; b) sand on sand layer, with comparison of results from 3D numerical FEM model (for a 50° slope and 5.1 L and for a 60° and 3.4 L); c) gravel on smooth surface; d) gravel on sand layer.

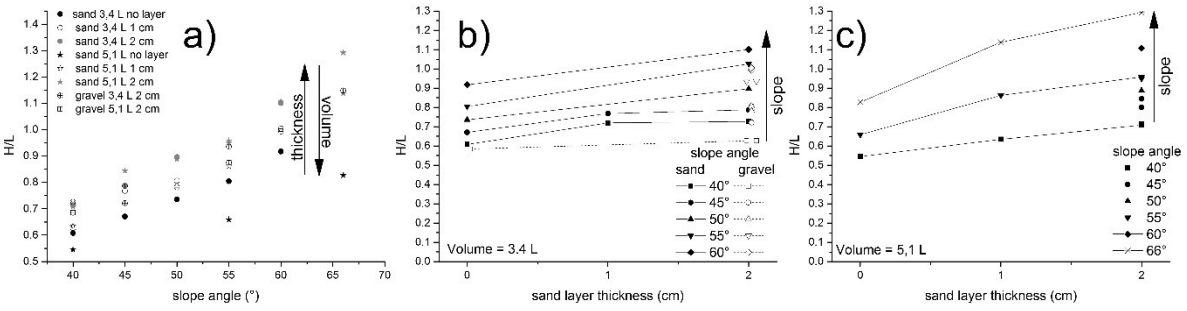

Figure 13. Drop height/maximum runout length ratio (Fahrboschung) plotted with respect to: a) the

slope angle for three different experimental conditions. This relationship also accounts for the fact that for constructional constraints, a greater slope also implies a higher drop height; b) and c) the sand layer thickness for different released volumes and materials; b) sand and gravel; c) only sand.

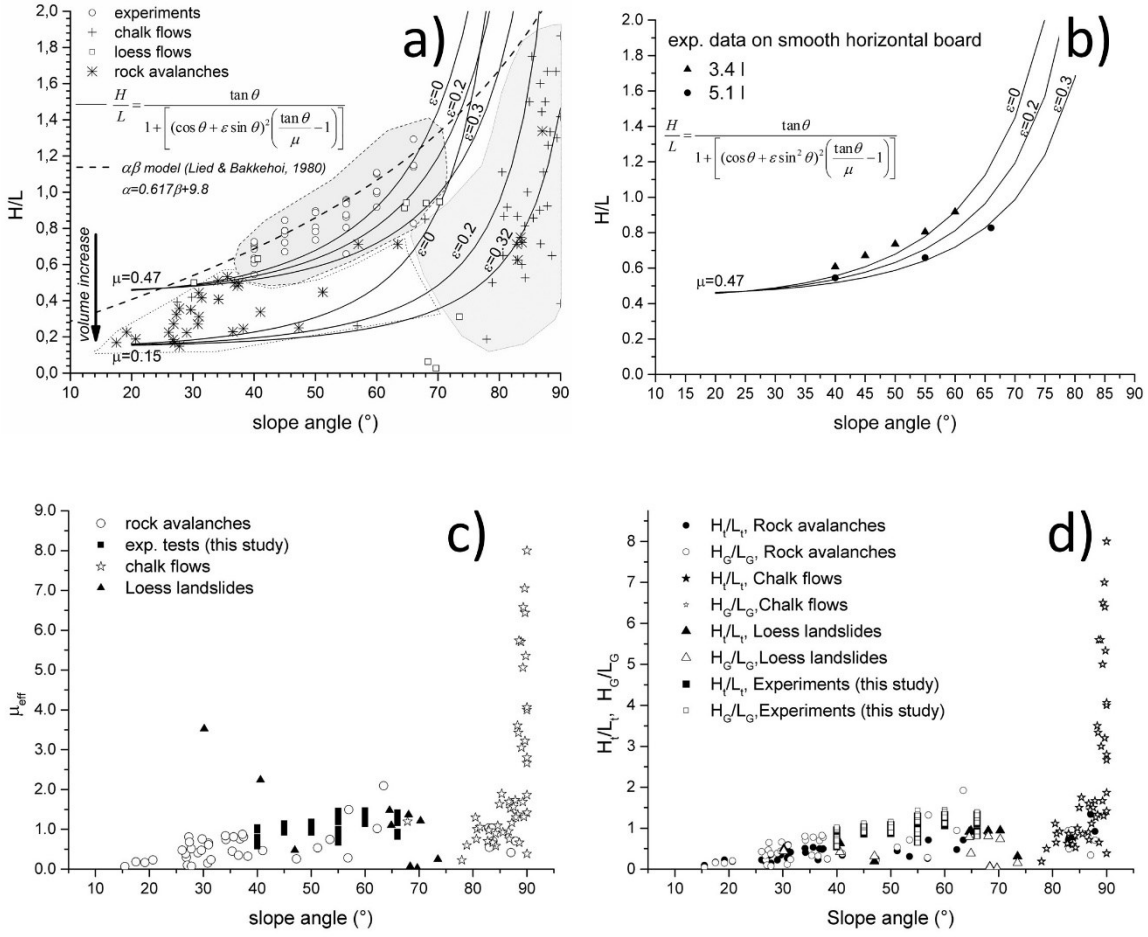

Figure 14. Figure 9 a) Results of the experiments (circles) together with data for real rock avalanches (stars, see Table S1 in Supporting Information) and chalk falls and flows on tidal flat (crosses, from Hutchinson, 2002; Duperret et al., 2006) and loess flowslides (Ma et al., 2014). The trend of the predictions of Eq. 1 with the indicated values of ε and μ are also reported. The case of ε=0 corresponds to the case by Okura (2000). The thick black line is the prediction of the $\alpha\beta$-model by Lied and Bakkehoi (1980) with K and B as in the legend; b) H/L versus slope angle data for experiments with Hostun sand propagating on an inclined slope and depositing on a smooth (i.e.

with no erodible layer) horizontal sector for two volumes of experimental sand (3.4 l and 5.1 l). Curves obtained by applying Eq. (3) for a fixed coefficient of friction and three different restitution coefficients are plotted.c) Results plotted in a larger scale for the effective friction coefficient as defined by Lucas et al. (2014); d): The same ratio as in a) but for the center of mass (H_G/L_G) in addition to the previous data.

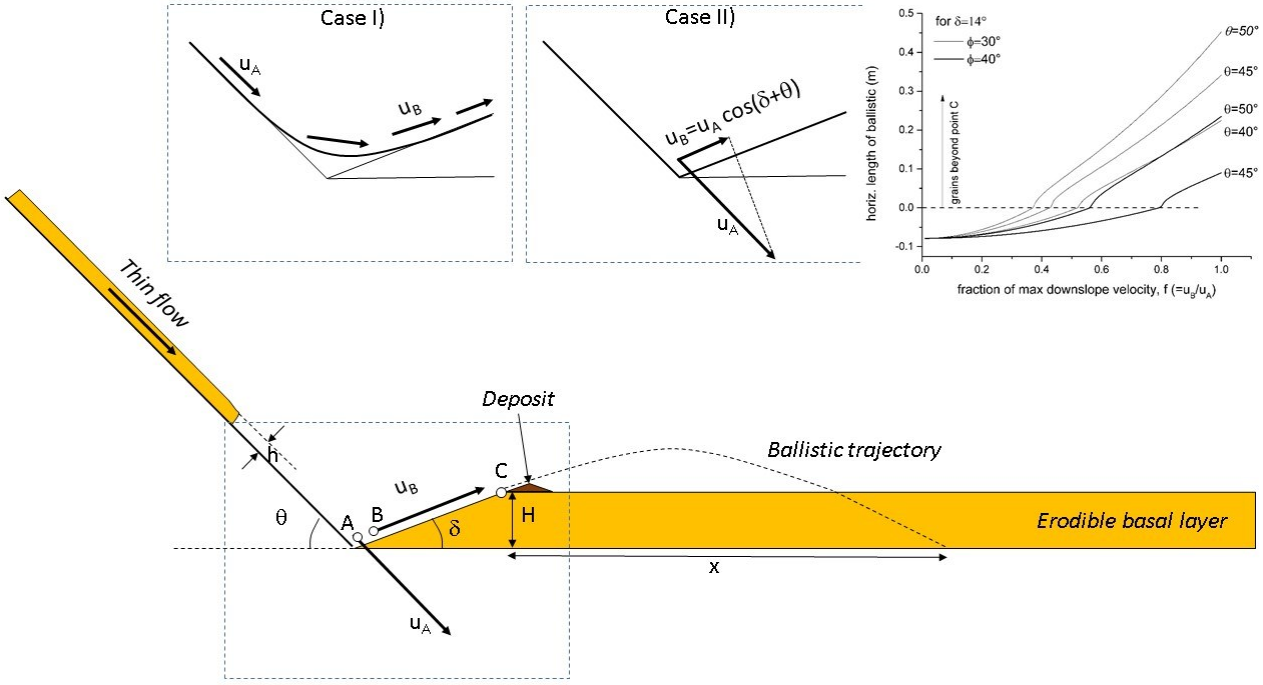

Figure 15. Geometrical conditions and possible cases for the calculation of the ballistic generation of the frontal wave. In contrast with other experimental and real conditions with fixed angle δ, in these experiments δ can change according to the erosion by and deposition of the flowing material. Case I) entry velocity fully preserved during the change in direction; Case II) exit velocity equal to the component parallel to the ramp excavated in the basal erodible layer by the flow. In both cases the initial velocity for ballistic trajectory results from upslope rise and friction action. Inset plot in the upper right corner represents the horizontal length of the ballistic trajectory at varying f for different values of ϕ (30°-40°) and θ (40°-50°) and a constant δ (14°). Dashed horizontal line represents the limit condition beyond which particles can fly ballistic beyond point C.

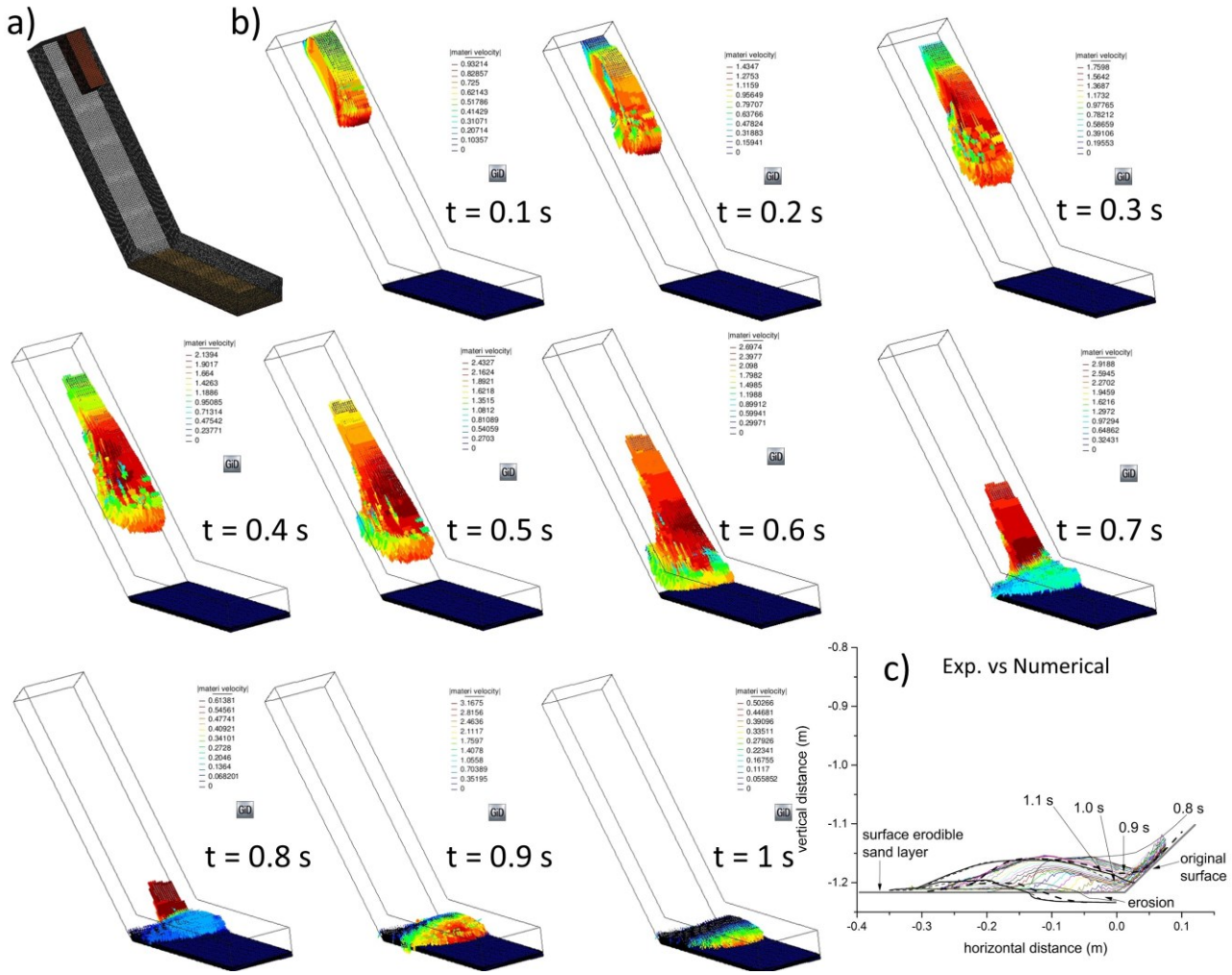

Figure 16. Three dimensional simulation for a test along a 50° slope, with 5.1 l of sand and a 2 cm thick basal layer (see also Fig. 1Sa-S1c). a) space discretization, b) Velocity vectors with colors scaled for each time step; c) material and erosion interface profiles at different time steps compared to the experiment.

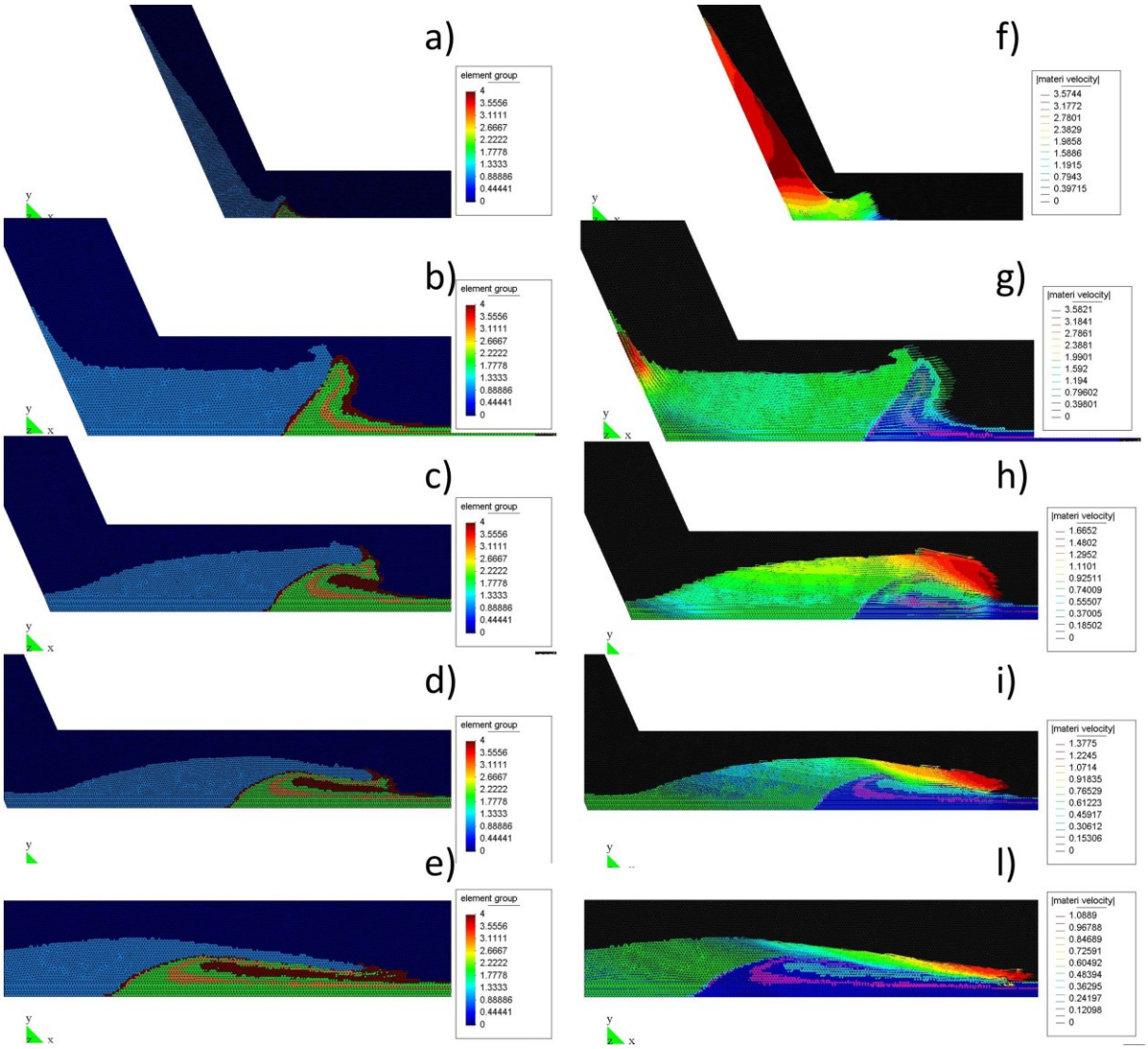

Figure 17. 2D FEM simulation of the test with layered sand layers as in Fig. 7. Orange layer as in fig. 7, whereas brown layer corresponds to blue layer in Fig. 7. a)-e) Material distribution and f)-l) velocity vectors for a FEM plane strain simulation for geometrical conditions (Fig. 2, for $\theta = 66°$) and physical mechanical properties (Table 1) as in the experimental tests. Legend for velocity vectors is rescaled at each time step. Layered erodible material is represented on the horizontal plane. Final front inclination: ca 11°.

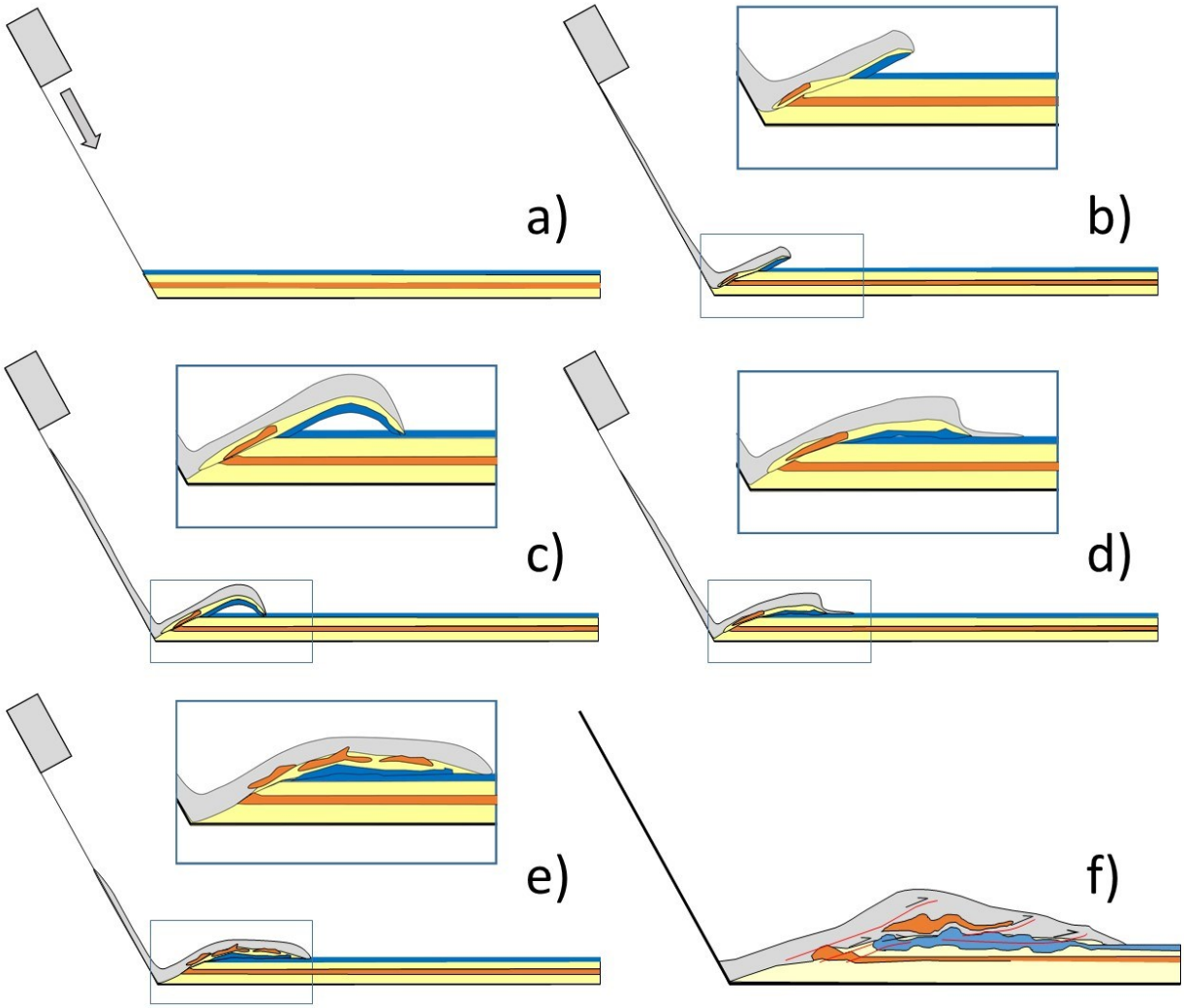

1077

1078 *Figure 18. Internal structures and kinematic interpretation of the erosion and deposition from the*
1079 *result of the experiments with colored sand layers. a)-e): sketches of the evolution of the colored*
1080 *layers and of the flow surface at different time steps. f): final distribution of the colored layers within*
1081 *the deposit (compare fig. 7 e and 17 f). For phases b) to e) enlargements of the sector (within the*
1082 *rectangular box) affected by erosion are shown.*

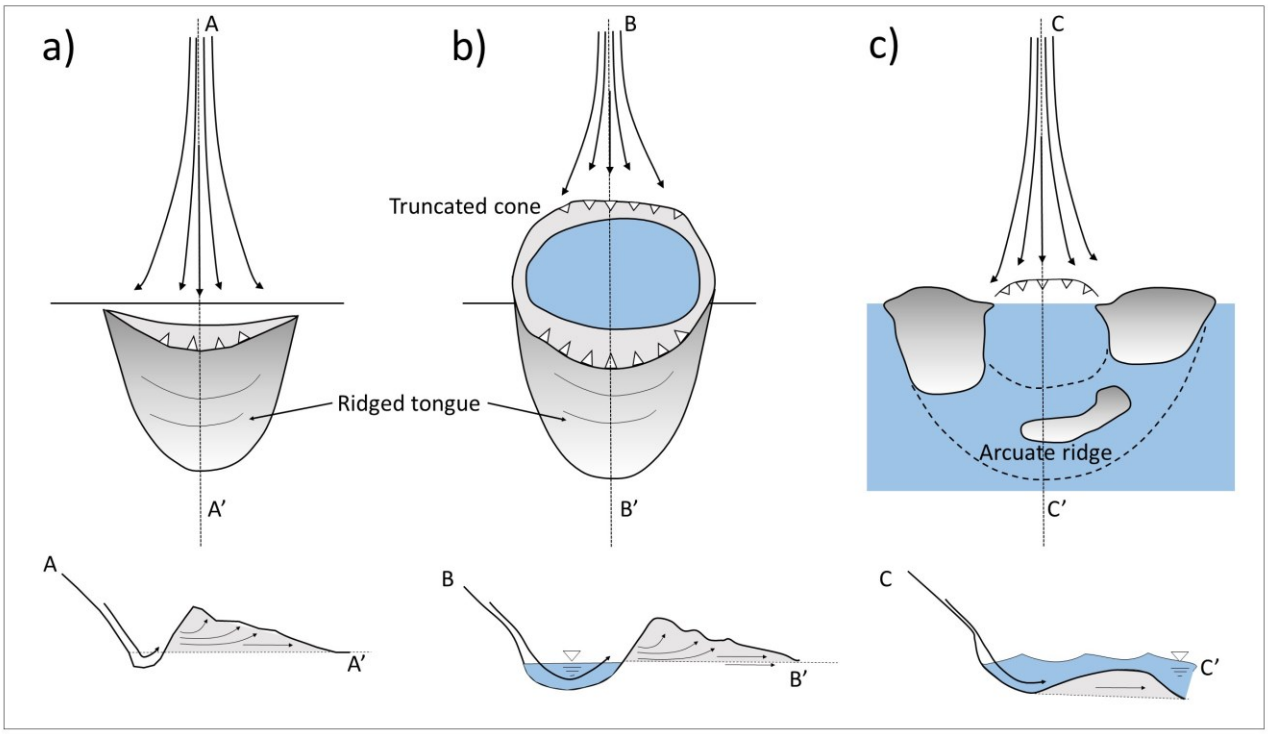

Figure 19. Three typologies of snow avalanche impact depressions in the Troms area of Norway according to Corner (1980). For each variety, the upper figure shows the scheme of formation, and the lower diagram an ideal cross-section. A: Tongue-like; B: pit; C: pool. In some cases, water fills up the depression (blue). From Corner (1980), modified.

Table 1. Properties of the granular materials used in the experiments. The terms smooth and sandy apply to the conditions of the horizontal deposition surface.

Material	Angle of repose (°)		Angle of avalanching (°)		Internal friction angle (°) direct shear test		Mean Bulk Density (g/cm^3)	Use in the experiments
	smooth	*sandy*	*smooth*	*sandy*	*peak*	*residual*		
Hostun sand	31	33	25.4	31.7	37.7	31	1.42 ±0.1	Erodible layer Granular flow
gravel	31	34	28.7	33.2	n.d	n.d.	1.53 ±0.1	Granular flow

Table 2. Summary of the different test conditions in terms of type of released and substrate material, thickness of the substrate sand layer, volume released and slope angle.

Released material	Substrate	Substrate thickness	VOLUME	Slope
		cm	litres	°
sand	smooth	0, 1, 2	1.6, 3.4, 5.1	40, 45, 50, 55, 60, 66
sand	sand	0, 1, 2	1.6, 3.4, 5.1	40, 45, 50, 55, 60, 66
gravel	smooth	0, 1, 2	1.6, 3.4, 5.1	40, 45, 50, 55, 60, 66
gravel	sand	0, 1, 2	1.6, 3.4, 5.1	40, 45, 50, 55, 60, 66

Table 3. List of the mathematical symbols used in this work and their meaning

Symbol	Meaning
B	Height of the granular flow in the release box
D	Thickness of the granular flow
D'	Thickness of the eroded layer
D_{MAX}	Maximum erodible thickness
f	Fraction of the velocity of one ballistic grain with respect to the initial velocity in the problem of ballistic jump (Eq. 13)
f_{CRIT}	Critical value of f
g	Gravity acceleration
H	Fall Height of the granular flow (or landslide)
H/L	Fahrboeschung
L	Runout of the granular flow (or landslide)
L′	Length of the sloping board
M	Mass of the granular flow
M'	Mass of the eroded material
R_H	Runout on the horizontal table without erosion
R_H^*	Runout on the horizontal table with erosion
S	Basal surface area of the granular flow
U_x	Horizontal velocity past the slope break
u_{entr}	Velocity of the granular flow after entrainment
u_0	Horizontal velocity at the slope break
X	Maximum horizontal distance of a grain in ballistic flight
x	Horizontal distance of the granular flow (meant as a variable)
δ	Angle of attack of the deposit in the evaluation of the
ΔL	Total runout measured along the real path
ε	Coefficient of restitution
μ	Friction coefficient
μ_{eff}	Effective friction coefficient (accounting also for the initial height of the granular material)
ρ	Density of granular flow
θ	Inclination angle of the board